

1 **Modern water/rock reactions in Oman hyperalkaline peridotite aquifers and implications**  
2 **for microbial habitability**

3

4 Hannah M. Miller<sup>a,\*</sup>, Jürg M. Matter<sup>b,c</sup>, Peter Kelemen<sup>c</sup>, Eric T. Ellison<sup>a</sup>, Mark E. Conrad<sup>d</sup>, Noah  
5 Fierer<sup>e,f</sup>, Tyler Ruchala<sup>g</sup>, Masako Tominaga<sup>g</sup>, and Alexis S. Templeton<sup>a\*</sup>

6 <sup>a</sup>Department of Geological Sciences, UCB 399, University of Colorado, Boulder, CO 80309,  
7 USA

8 <sup>b</sup>Department of Ocean and Earth Science, University of Southampton, UK SO14 3ZH

9 <sup>c</sup>Lamont-Doherty Earth Observatory of Columbia University, 61 Route 9W, Palisades, NY  
10 10964, USA

11 <sup>d</sup>Earth Sciences Division, MS 70A-4418, E.O. Lawrence Berkeley National Laboratory,  
12 Berkeley, CA 94720, USA

13 <sup>e</sup>Department of Ecology and Evolutionary Biology, CIRES 215,-University of Colorado,  
14 Boulder, CO 80309, USA

15 <sup>f</sup>Cooperative Institute for Research in Environmental Sciences, University of Colorado, Boulder,  
16 CO 80309

17 <sup>g</sup>Department of Geology and Geophysics, Texas A&M University, College Station, TX 77843,  
18 USA

19 \*Corresponding author. Tel.: +1 303.492.6174 *E-mail address:* [hannah.miller-1@colorado.edu](mailto:hannah.miller-1@colorado.edu)

20 \*Co-corresponding author. Tel: +1 303.735.6069 *E-mail address:*

21 [alexis.templeton@colorado.edu](mailto:alexis.templeton@colorado.edu)

22 **Abstract:**

23 The Samail ophiolite in Oman is undergoing modern hydration and carbonation of peridotite and  
24 may host a deep subsurface biosphere. Previous investigations of hyperalkaline fluids in Oman  
25 have focused on fluids released at surface seeps, which quickly lose their reducing character and  
26 precipitate carbonates upon contact with the O<sub>2</sub>/CO<sub>2</sub>-rich atmosphere. In this work, geochemical  
27 analysis of rocks and fluids from the subsurface provides new insights into the operative  
28 reactions in serpentinizing aquifers. Serpentinite rock and hyperalkaline fluids (pH >10), which  
29 exhibit millimolar concentrations of Ca<sup>2+</sup>, H<sub>2</sub> and CH<sub>4</sub>, as well as variable sulfate and nitrate,  
30 were accessed from wells situated in mantle peridotite near Ibra and studied to investigate their  
31 aqueous geochemistry, gas concentrations, isotopic signatures, mineralogy, Fe speciation and  
32 microbial community composition.

33 The bulk mineralogy of drill cuttings is dominated by olivine, pyroxene, brucite, serpentine and  
34 magnetite. At depth, Fe-bearing brucite is commonly intermixed with serpentine, whereas near  
35 the surface, olivine and brucite are lost and increased magnetite and serpentine is detected.  
36 Micro-Raman spectroscopy reveals at least two distinct generations of serpentine present in drill  
37 cuttings recovered from several depths from two wells. Fe K-edge x-ray absorption near-edge  
38 spectroscopy (XANES) analysis of the lizardite shows a strong tetrahedral Fe coordination,  
39 suggesting a mixture of both Fe(II) and Fe(III) in the serpentine. Magnetite veins are also closely  
40 associated with this second generation serpentine, and 2-10µm magnetite grains overprint all  
41 minerals in the drill cuttings. Thus we propose that the dissolved H<sub>2</sub> that accumulates in the  
42 subsurface hyperalkaline fluids was evolved through low temperature oxidation and hydration of  
43 relict olivine, as well as destabilization of pre-existing brucite present in the partially  
44 serpentinized dunites and harzburgites. In particular, we hypothesize that Fe-bearing brucite is  
45 currently reacting with dissolved silica in the aquifer fluids to generate late-stage magnetite,  
46 additional serpentine and dissolved H<sub>2</sub>.

47 Dissolved CH<sub>4</sub> in the fluids exhibits the most isotopically heavy carbon in CH<sub>4</sub> reported in the  
48 literature thus far. The CH<sub>4</sub> may have formed through abiotic reduction of dissolved CO<sub>2</sub> or  
49 through biogenic pathways under extreme carbon limitation. The methane isotopic composition  
50 may have also been modified by significant methane oxidation. 16S rRNA sequencing of DNA  
51 recovered from filtered hyperalkaline well fluids reveals an abundance of *Meiothermus*,  
52 *Thermodesulfovibrionaceae* (sulfate-reducers) and *Clostridia* (fermenters). The fluids also  
53 contain candidate phyla OP1 and OD1, as well as *Methanobacterium* (methanogen) and  
54 *Methylococcus* sp. (methanotroph). The composition of these microbial communities suggests  
55 that low-temperature hydrogen and methane generation, coupled with the presence of electron  
56 acceptors such as nitrate and sulfate, sustains subsurface microbial life within the Oman  
57 ophiolite.

## 1. Introduction

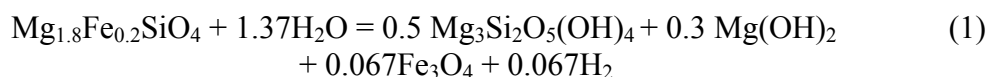
The Samail ophiolite in the Sultanate of Oman, the largest and best exposed ophiolite sequence on Earth, is well-suited to the study of low temperature serpentinization, which is the aqueous alteration of ultramafic rocks. Over 15,000 km<sup>3</sup> of peridotite is currently undergoing low temperature hydration and oxidation (Barnes et al., 1978; Neal and Stanger, 1983; Neal and Stanger, 1985; Clark and Fontes, 1990; Kelemen and Matter, 2008; Kelemen et al., 2011; Streit et al., 2012; Paukert et al., 2012). Modern serpentinization is inferred from the distribution of hyperalkaline seeps that release hyperalkaline fluids rich in H<sub>2</sub> and CH<sub>4</sub>, and poor in dissolved inorganic and organic carbon. However, the water/rock reaction pathways giving rise to H<sub>2</sub> and methane formation at near-surface temperatures are not known. Moreover, no studies have yet explored whether the active hydrogeochemical system hosts a subsurface biosphere.

In Oman, the mantle peridotite consists of olivine, orthopyroxene, and serpentine, with trace amounts of calcic pyroxene, chromite, and Fe-oxides (Hanghøj et al., 2010). The mantle peridotite is 30-70% serpentinized (Boudier et al., 2010) and variably carbonated. Some serpentinization occurred during hydrothermal circulation when the ophiolite was situated at an oceanic spreading ridge, some during thrust emplacement of the ophiolite over pelagic and continental margin sediments, some during late Cretaceous sub-aerial weathering and a subsequent marine transgression, and some during ongoing water/rock reactions (Hanghøj et al., 2010; Kelemen et al., 2011). The proportions and spatial distribution of serpentine and other secondary minerals formed during these different events are unclear. Completely unaltered peridotite is not observed in outcrop in Oman, but the least altered samples are found in deep canyons, whereas the most serpentinized outcrops are in areas of low relief (Kelemen et al., 2011). The peridotite also undergoes carbonation reactions as evidenced by modern carbonate vein and terrace dates (Clark and Fontes, 1990; Kelemen and Matter, 2008; Mervine et al., 2014) which indicate temperatures of formation from 30-60°C (Kelemen et al., 2011; Streit et al., 2012).

An active hydrological system drives present-day serpentinization and other alteration processes occurring in the subsurface. Groundwater circulation in the peridotite aquifer is controlled by fissure and fracture hydraulic conductivity. Near-surface fissures (perhaps extending to ~ 50 meters depth) accommodate most of the groundwater flow with a hydraulic conductivity of 10<sup>-7</sup> m/s (Dewandel et al., 2005). The origins of this shallow, hydraulically active zone are not clear, but are probably due to meteoric weathering. The peridotite aquifer contains a network of fractures that began to develop when the ophiolite was hydrothermally altered at the mid-ocean ridge, ~95 million years ago during the Middle Cretaceous (Coleman, 1981). The fractures in the peridotite host serpentine and carbonate veins (Dewandel et al., 2005). Hyperalkaline surface seeps generally discharge at the contact between the mantle and overlying crustal rocks, and along the basal thrust plane of the ophiolite sequence. They release high pH fluids (>11) rich in Ca<sup>2+</sup>, OH<sup>-</sup>, H<sub>2</sub>, and CH<sub>4</sub>. The surrounding mineralogy is dominated by carbonates that precipitated when the carbon deprived fluids mixed with atmospheric CO<sub>2</sub> (Kelemen and Matter, 2008; Kelemen et al., 2011; Paukert et al., 2012; Chavagnac et al., 2013; Chavagnac et al., 2013).

104 The origin of dissolved H<sub>2</sub> and CH<sub>4</sub> in Oman are enigmatic. Currently, there is no evidence for  
105 modern hydrothermal activity at temperature greater than 200°C of water/rock reactions in the  
106 peridotite aquifer, which would correspond to a depth of ~8 km based on a geothermal gradient  
107 of 25°C/km. Although serpentinization processes have been extensively studied at temperatures  
108 >120°C, the mineral assemblages and alteration processes leading to formation of dissolved H<sub>2</sub>  
109 and CH<sub>4</sub> during serpentinization at lower temperatures are poorly constrained.

110  
111 Serpentinization leads to the evolution of hydrogen through hydration and the oxidation of  
112 reduced iron species found in olivine and pyroxenes. For typical mantle olivine with molar  
113 Mg/(Mg+Fe) = 0.9, a simplified reaction above 200°C might be:



114  
115  
116  
117  
118 (e.g. Equation 1; Frost, 1985; McCollom and Bach, 2009). Such water/rock reactions produce  
119 fluids rich in H<sub>2</sub>. These fluids also commonly contain abundant dissolved CH<sub>4</sub>, which may form  
120 abiogenically as the result of Fischer-Tropsch Type or Sabatier reactions (Horita and Berndt,  
121 1999; Etiope et al., 2013), or biologically via methanogenesis (Balch et al., 1979; Sleep et al.,  
122 2004).

123  
124 Hydrogen generation during serpentinization has been modeled from 8-400°C (McCollom and  
125 Bach, 2009; Okland et al., 2012; Klein et al., 2013). Experimentally produced H<sub>2</sub> has been  
126 generated from 0-100°C (Stevens and McKinley, 1995; Anderson et al., 1998; Stevens and  
127 McKinley, 2000; Neubeck et al., 2011; Okland et al., 2012; Mayhew et al., 2013) Comparisons  
128 of model and experimental results often yield conflicting results, perhaps because of assumptions  
129 included in models. For example, McCollom and Bach (2009) utilize reaction path models to  
130 simulate water-rock reactions and resulting mineral assemblages, but they are constrained by the  
131 lack of existing thermodynamic data for Mg:Fe solid solutions, the incorporation of Fe(III) into  
132 secondary silicates, and the lack of data on mineral compositions that form at low temperature.  
133 Also, models assume the reactions have reached equilibrium, and it is unlikely that low-  
134 temperature laboratory experiments are fully equilibrated. Thus, detailed analysis of field  
135 samples from low-temperature serpentinizing environments is required to ground-truth modeling  
136 efforts.

137  
138 There is also a lack of data on the detection or characterization of microorganisms in Oman's  
139 hyperalkaline aquifers. The high concentrations of H<sub>2</sub> and CH<sub>4</sub> in the hyperalkaline fluids  
140 provide electron donors that could be utilized by subsurface chemolithoautotrophic life, which  
141 could contribute to carbon cycling in the subsurface (Stevens and McKinley, 1995; Sleep et al.,  
142 2004, p.2005; Nealson et al., 2005; Mayhew et al., 2013; Klein et al., 2015). The search for  
143 microbial life in other serpentinizing environments has primarily been focused on sequencing the  
144 16S rRNA gene from easily accessible surface springs as windows into the subsurface (Neal and  
145 Stanger, 1983; Abrajano et al., 1990; Bruni et al., 2002; Meyer-Dombard et al., 2015;  
146 Woycheese et al., 2015), although recent work by Postec et al. (2015) isolated DNA from  
147 carbonate chimneys from a low-temperature hydrothermal field. However, all these studies were  
148 limited to surface samples collected in oxygenated environments, which allows aerobic

149 organisms to flourish. It is unclear if the microbes inhabiting the surface seeps are similar to  
150 those active in the anaerobic subsurface.

151  
152 This study was designed to assess low temperature serpentinization processes in a peridotite  
153 aquifer in Oman and to determine what types of microbial life are hosted in the subsurface. We  
154 sampled hyperalkaline, H<sub>2</sub>-, CH<sub>4</sub>-rich fluids from 10-300 m depth in peridotite and studied their  
155 geochemistry, gas concentrations and isotopic signatures. We integrated these data with  
156 mineralogical and spectroscopic analysis of mineral chips recovered from depth within two  
157 peridotite wells to elucidate the oxidation state, mineralogy, and extent of serpentinization of the  
158 rocks in contact with deep subsurface fluids. Magnetic hysteresis analyses on downhole bulk  
159 rock samples augment these geochemical and mineralogical analyses by providing the  
160 distribution of different rock magnetic properties within drilled sections, thereby suggesting  
161 possible zonation in the serpentinization process. Geochemical data were complemented by high  
162 throughput 16S rRNA sequencing of DNA recovered from the well fluids to identify microbial  
163 organisms present in the fluid. These data provide the first insights into the modern water/rock  
164 reactions in a hyperalkaline Oman aquifer, and the potential coupling between geochemical and  
165 microbiological processes during low-temperature serpentinization.

166

167

168 **2. Methods**

169 *2.1 Field methods*

170 The Ministry of Water Resources of the Sultanate of Oman drilled numerous wells into peridotite  
171 (~300 meters deep) to investigate water resources for the region. Water samples and drill  
172 cuttings were obtained from wells NSHQ14 and NSHQ04 in a peridotite plain in the Samail  
173 ophiolite, Oman (Figure 1). NSHQ04 is near a north/south trending fault, with gabbro to the west  
174 and mixed dunite and gabbro lenses cut by pyroxenite dikes to the east. NSHQ14 is several  
175 kilometers from the crust-mantle boundary; the surrounding rocks are mainly harzburgite with  
176 meter-scale dunite bands.

177 In January 2014, a shallow submersible pump was used to collect water from 18 meters depth in  
178 both NSHQ04 and NSHQ14, and a stainless steel bailer was used to collect water from 260  
179 meters in well NSHQ14. Water samples containing dissolved gases were collected in sterile  
180 syringes and injected into N<sub>2</sub>-purged vials and later used for headspace gas analysis. The vials  
181 were acid washed, autoclaved and baked at 400°C in a muffle furnace prior to field work.  
182 Samples for ICP-MS analysis were filtered with 0.2µm Millipore filters and acidified in the field  
183 with concentrated nitric acid to ~pH 2. The fluid pH, temperature, and conductivity were  
184 measured with a conductivity meter (YSI Model#85/10) while pH was measured with a Mettler-  
185 Toledo SevenGo2 pH meter calibrated with reference standards of pH 12.46, 10.01, and 7.

186 Fluids (~5-10L) from the wells were pumped and filtered through 0.2µm Sterivex inline filters to  
187 recover biomass for DNA extraction. Filters were transported frozen in liquid nitrogen and stored  
188 in a -70°C freezer until extraction.

189 We also obtained drill cuttings (rock chips recovered during drilling) of the wells from 262, 140,  
190 70, and 17 meters depth at NSHQ14 and from 303, 180, and 120 meters depth at well NSHQ04.  
191 These were mounted in epoxy and prepared as 30mm thick polished thin sections for analysis.

192 *2.2 Laboratory methods*

193 Major cations (Mn<sup>2+</sup>, Fe<sup>2+</sup>, Mg<sup>2+</sup>, Ca<sup>2+</sup>, Al<sup>3+</sup>), SiO<sub>2</sub>, and trace elements (Ni, As, Se, Cu, Cd, Zn  
194 Co, Cr) were analyzed on field-acidified and filtered well waters using Inductively Coupled  
195 Plasma-Mass Spectrometry (ICP-MS) on a ThermoScientific X Series 2. Major anions (F<sup>-</sup>, Cl<sup>-</sup>,  
196 Br<sup>-</sup>, NO<sub>3</sub><sup>-</sup>, PO<sub>4</sub><sup>3-</sup>, SO<sub>4</sub><sup>2-</sup>) were analyzed using Ion Chromatography (IC) on a Dionex IC25 with an  
197 IonPac column and a 9 mM sodium carbonate eluent. Water samples were collected in acid-  
198 washed, autoclaved, and ashed organic free vials and sent to NASA Ames Research Center to  
199 measure low weight molecular organic acids on a Shimadzu Prominence LC20AT high-  
200 performance liquid chromatograph (HPLC) equipped with a SPD-M20A photodiodearray  
201 detector and a flow rate of 1mL per minute.

202  
203 Drill cuttings were powdered with a mortar and pestle and then x-ray diffraction (XRD) data  
204 were obtained using CuKα radiation ( $\lambda = 1.5418\text{\AA}$ ) in the range 15-65° 2θ using a Bruker D2  
205 Phaser operated at 30 kV and 10 mA. A Lynxeye 1D detector with a step size of 0.02° and  
206 collection time of 1 s per step were employed. The XRD spectra were semi-quantitatively fit  
207 using the Bruker DiffracEva program and results were compared to the RRUFF database (Downs  
208 2006).

209  
210 To determine H<sub>2</sub> and CH<sub>4</sub> concentrations (detection limit of 10ppm and analytical error of 5%) in  
211 the gases exsolved from the well fluids, we used a SRI 8610C gas chromatograph (GC) with a  
212 2m by 1mm ID micropacked ShinCarbon ST column with N<sub>2</sub> as the carrier gas. 0.5mL of gas  
213 was sampled from the headspace of serum vials sealed with blue rubber stoppers and was  
214 injected into a sampling port on the GC. H<sub>2</sub> was measured with a thermal conductivity detector  
215 (TCD), and a flame ionization detector (FID) was concurrently used to measure CH<sub>4</sub>.

216  
217 Stable isotope analyses were conducted at the Center for Isotope Geochemistry at the Lawrence  
218 Berkeley National Laboratory. The isotopic compositions of H<sub>2</sub> and CH<sub>4</sub> were analyzed using a  
219 Thermo Scientific GC Trace Gas Ultra system connected to a Thermo Scientific Delta V Plus  
220 Mass Spectrometer (IRMS). Gas samples were injected into a 6-port valve (the loop size varied  
221 from 5L to 250 L depending on the concentration of the analyte in the sample) bypassing the  
222 inlet of the GC. After flushing with at least 3 times the volume of the loop, the sample was  
223 injected into the GC where the gases were separated chromatographically on an HP-molesieve  
224 fused silica capillary column (30 m x 0.320 mm). For H<sub>2</sub>, after the samples went through the GC,  
225 they were passed through a combustion furnace at room temperature and then into the IRMS.  
226 Reproducibility of these analyses is ±2.5‰ (1s), as determined by repeated analyses of a  
227 laboratory gas standard. Carbon isotope ratios of CH<sub>4</sub> were analyzed using the same system with  
228 with the combustion furnace (a capillary ceramic tube loaded with Ni, Cu, and Pt wires) set at  
229 1030 °C where the CH<sub>4</sub> was converted to CO<sub>2</sub>. Produced water was removed, and the carbon  
230 isotope ratio of the resulting CO<sub>2</sub> was measured in the IRMS. The reproducibility of these  
231 analyses is ±0.2‰. For hydrogen isotopes of CH<sub>4</sub>, the sample was passed through a pyrolysis  
232 furnace at 1450 °C and the resulting H<sub>2</sub> gas measured with the IRMS. The reproducibility of  
233 these analyses is ± 5‰.

234  
235 Samples with 10-100 micrograms calcite were reacted with 100% H<sub>3</sub>PO<sub>4</sub> at 90°C and then used  
236 for both carbon and oxygen isotope analyses (δ<sup>13</sup>C and δ<sup>18</sup>O), which were determined using a  
237 GV IsoPrime mass spectrometer with Dual-Inlet and MultiCarb systems in the Center for Stable  
238 Isotope Biogeochemistry (CSIB) at Department of Integrative Biology, University of California  
239 at Berkeley. Several replicates of one international standard NBS19, and two lab standards  
240 CaCO<sub>3</sub>-I & II were measured along with samples for each run. The overall external analytical  
241 precision is about ±0.05‰ for δ<sup>13</sup>C and about ±0.07‰ for δ<sup>18</sup>O.

242  
243 The isotopic compositions of the water samples were measured using CIG's Los Gatos Research  
244 Liquid Water Isotope Analyzer (LWIA). 1 ml of each sample was loaded into 2 ml vials. Using  
245 an auto sampler, each sample was injected into the LWIA 8 times where the data for the first 3  
246 injections were discarded and the data for the remaining 5 injections averaged to give the raw  
247 isotope values. The data were then compared to a series of 3 standards bracketing the expected  
248 isotopic values of the samples analyzed and run multiple times throughout the run. The  
249 reproducibility of these analyses based on repeated analyses of the standards is better than ±1‰  
250 for δD and ±0.2‰ for δ<sup>18</sup>O.

251  
252 **2.3 Microscale analytical techniques**

253

254 Synchrotron-based hard X-ray measurements of Fe K-edge micro-x-ray absorption near edge  
255 spectra ( $\mu$ XANES) were conducted at Beamline 2-3 at the Stanford Synchrotron Radiation  
256 Lightsource (SSRL). The incident energy was selected with a Si (111) double crystal  
257 monochromator with the SPEAR accelerator ring containing  $\sim$ 150-200mA at 3.0 GeV. The beam  
258 was focused to approximately 2 by 2  $\mu$ m using Kirkpatrick Baez mirrors. Data were collected at  
259 the Fe K-edge using a Fe<sup>0</sup> foil calibration of 7112 eV with a single-element Vortex detector  
260 capable of reading several million counts per second.

261  
262 Fe K-edge mapping was conducted at 8 energies (7123, 7126, 7128, 7129, 7130, 7131, 7133  
263 keV) chosen to maximize the differences in normalized intensity between representative XANES  
264 (Mayhew et al., 2011; Mayhew et al., 2013). These data were coupled with an 11 keV map of  
265 trace element distribution to identify unique areas in the sample. Principle Components Analysis  
266 (PCA) on these multiple energy XRF maps were used to identify the location of unique Fe  
267 species in the map area using Sam's Microprobe Analysis Kit (SMAK). We then collected  
268 representative  $\mu$ XANES spectra from those spots and employed PCA to identify key end  
269 member  $\mu$ XANES spectrum that represent the unique chemical forms of Fe in each sample.  
270 Finally, multiple-energy maps were fit with the fluorescence intensities of each end member  
271 mXANES spectra to show the distribution of Fe-bearing minerals in complex reacted and  
272 unreacted samples.

273  
274 XANES were normalized with Sam's Interface for XAS Package (SIXPACK). XANES spectra  
275 were collected from a range of 6882-7152eV. To qualitatively determine Fe speciation and  
276 mineralogy, spectra were fit from 7110 to 7150 eV using least squares fitting of Fe model  
277 compounds (in SIXPACK) calibrated using the first inflection of a Fe<sup>0</sup> foil at 7112 eV (Mayhew  
278 et al., 2011). We also collected the pre-edge (7108-7118eV) region with a step size of 0.1eV and  
279 dwell time of 3 seconds and analyzed the pre-edge employing protocols by Andreani *et al.*  
280 (2013) and Wilke *et al.* (2001) to determine the ratio of Fe<sup>2+</sup>/Fe<sup>3+</sup> in the various generations of  
281 serpentine.

282  
283 Beamline 4-1 at SSRL was used to collect bulk Fe K-edge spectra for seven powdered well chip  
284 samples. A Si (220)  $\phi=0$  monochromator was used and X-ray absorption spectra (XAS) were  
285 collected on a Lytle detector. A Fe<sup>0</sup> foil standard was used and calibrated to 7112eV. Duplicate  
286 spectra were collected and averaged for XANES scanning from a range of 6882-7082eV with a  
287 step size of 10 points, then from 7092 to 7520 with a 0.35 step size.

288  
289 Quantum Design MPMS Superconducting Quantum Interface Device (SQUID) magnetometer  
290 with the magnetic moment resolution of  $10^{-8}$  emu at Department of Physics and Astronomy at  
291 Michigan State University was used to analyze bulk rock powder samples to determine magnetic  
292 hysteresis parameters. A total of 7 samples with various weights (40-259 mg) are measured over  
293 the range of  $\pm$  5 T at 300K.

294  
295 Micro-Raman spectra and hyperspectral maps for well rock chip samples were collected using a  
296 Horiba LabRAM HR Evolution Raman spectrometer equipped with a 532nm frequency-doubled  
297 Nd:YAG laser (Laser Quantum, Torus 532 + mpc3000) coupled to an Olympus BXFM optical  
298 microscope. The laser beam was focused through a 50x objective lens, yielding a spatial  
299 resolution of  $\sim$ 2 $\mu$ m. A 600 lines/mm grating and adjustable confocal pinhole (100  $\mu$ m-200  $\mu$ m)



300 was used to give a spectral resolution full width at half maximum (FWHM) of 4.5-8.4  $\text{cm}^{-1}$ .  
301 Spectra were collected from 20-1200 $\text{cm}^{-1}$  using a Si-based CCD detector (1024 x 256 pixels).  
302 The spectrometer was calibrated using the 520  $\text{cm}^{-1}$  Raman peak of Si daily prior to analysis.  
303 Spectral data were corrected for instrumental artifacts and baseline-subtracted using a  
304 polynomial fitting algorithm in LabSpec 6 (Horiba Scientific). For the Raman microspectroscopy  
305 analyses, the drill cuttings from each depth in NSHQ14 and NSHQ04 were analyzed by  
306 generating hyperspectral maps of representative areas in the thin sections, using Multivariate  
307 Curve Resolution-Alternating Least Squares (MCR-ALS) and non-negativity constraints on  
308 scores and loadings to determine the main spectral components present, then collecting spot  
309 Raman spectra to verify the components, and fitting the hyperspectral data set with the end  
310 member spectra to generate component maps.

311  
312 Quantitative chemical analysis of serpentine was performed using the electron microprobe  
313 laboratory at the University of Colorado at Boulder on the JEOL JXA-8600 equipped with 4  
314 wavelength-dispersive spectrometers, and a PGT energy-dispersive spectrometer. Spot analyses  
315 of polished thin sections were performed at a current of 10 nA, accelerating voltage of 15 keV,  
316 and beam diameter of 10  $\mu\text{m}$  to avoid destroying the hydrated serpentine sample to analyze the  
317 major element compositions of Si, Al, Mg, Na, Ca, Cr, K, Fe, Mn, and Ti, using natural  
318 standards.

319  
320 TGA measurements were taken in a NETZSCH STA 449 F1 Jupiter. Between 60 and 110 mg of  
321 sample in an alumina crucible and a blank alumina crucible were heated in Argon up to 1000°C  
322 at a ramp rate of 10 Kelvin per minute. The crucibles were then held at 1000°C for one hour, at  
323 which point data collection stopped and the furnace cooled. The derivatives of the data were  
324 determined using NETZSCH Proteus.

#### 325 **2.4 16S rRNA sequencing**

326  
327 The microbial analyses were conducted as described previously (Bowers et al., 2013; Emerson et  
328 al., 2015). DNA was extracted from one quarter of each of the filter samples using the MoBio  
329 PowerSoil kit. The V4-V5 region of the 16S rRNA gene was PCR amplified in triplicate  
330 reactions using the 515f/806r primer pair. The primers contained the appropriate Illumina  
331 adapters and the reverse primer contains a 12-bp error-correcting barcode unique to each sample.  
332 The triplicate reactions were composited, amplicon concentrations were determined using the  
333 PicoGreen dsDNA assay, and the amplicons from all samples were pooled together in equimolar  
334 concentrations. Sequencing was conducted on an Illumina MiSeq at the University of Colorado  
335 Genomics Core Facility following the 2 × 250 bp paired-end protocol. Quality filtering of reads  
336 and processing of the reads was conducted as described in Barberán et al. (2015). After  
337 demultiplexing, reads were quality filtered at an equivalent sequencing depth (6000 reads per  
338 sample) and clustered into phylotypes using the UPARSE pipeline (Edgar, 2013). Reads were  
339 assigned to phylotypes at the  $\geq 97\%$  sequence similarity threshold and phylotype taxonomy was  
340 determined using the RDP classifier with a confidence threshold of 0.5 (Wang et al., 2007)  
341 trained on the Greengenes 13\_8 database (McDonald et al., 2012). Multivariate statistical  
342 analysis was performed in R, a software environment for statistical computing and graphics (R  
343 Development Core Team, 2008).

344  
345

### 346 3. Results

#### 347 3.1 Aqueous geochemistry of wells

348 Fluids were collected from two wells drilled into peridotite, NSHQ14 (up to a depth of 260m)  
349 and NSHQ04 (up to a depth of 50m, below which the well is collapsed). Minimum  
350 concentrations of dissolved H<sub>2</sub> and CH<sub>4</sub> were determined by GC. For NSHQ14 at 262m, some  
351 gas was lost from the fluids during the transfer from the bailer sampler to gas-tight vials due to  
352 rapid exsolution. The calculated dissolved H<sub>2</sub> concentrations range from 0.18 to 0.67 mM H<sub>2</sub>,  
353 and the methane concentrations range from 0.17 to 1.44 mM (Table 1).

354 The fluids in both wells are hyperalkaline: NSHQ14 has a pH of 11.5 and NSHQ04 has a pH of  
355 10.6. Major cation and anion analysis for fluids reveals >6mM Ca<sup>2+</sup>, ≥0.005mM Mg<sup>2+</sup>, and 6.75-  
356 12.30mM Na<sup>+</sup> (Table 1). Low molecular weight organic acids (lactate, acetate, formate,  
357 propionate, butyrate and valerate) are below detection limits of ~5.0 μM; thus, there is low  
358 dissolved organic carbon in the fluid. Dissolved inorganic carbon (DIC) levels for samples  
359 collected from these wells in 2012 were 0.078-0.391 mM (Paukert et al., 2012). Both wells  
360 contain high concentrations of Cl<sup>-</sup> (>20 mM), which are almost two orders of magnitude higher  
361 than the 0.35 mM Cl<sup>-</sup> present in Oman rainwater (Weyhenmeyer, 2000; Paukert et al., 2012). The  
362 well fluids contain 0.05-0.48 mM SO<sub>4</sub><sup>2-</sup> and 0.012-0.022 mM NO<sub>3</sub><sup>-</sup>. The trace element chemistry  
363 of the wells is similar; Ni and Cr are the most abundant metals (average of 0.15 and 0.18 μM,  
364 respectively. The only notable difference is NSHQ14 at 262m has more Zn (0.139 μM versus  
365 ~0.03 μM) than the other depths.

366 The fluids in the peridotite wells exhibit similar pH and aqueous geochemistry to surface alkaline  
367 springs previously sampled in Oman (Paukert et al., 2012); however, the NSHQ14 and NSHQ04  
368 well fluids contain more Ca<sup>2+</sup>, Cl<sup>-</sup>, NO<sub>3</sub><sup>-</sup> and generally SO<sub>4</sub><sup>2-</sup>. The dissolved silica concentrations  
369 are ~0.01mM SiO<sub>2(aq)</sub> versus the 0.04mM found in the surface seeps.

370 Oxidation-reduction potential (ORP) values were measured during the January 2012 field season.  
371 NSHQ14 fluids exhibit much higher ORP values (-31.6 mV) near the surface at 18 meter,  
372 whereas the fluids at 260m are highly reducing (-597.3 mV). The ORP value for fluids collected  
373 from NSHQ04 at 70 meters was -103.4 mV.

#### 374 3.2 Isotopic composition of fluids, dissolved gases, and carbonates

375 The δD values of dissolved H<sub>2</sub> are very low (-680‰ and -686‰ for NSHQ04 and NSHQ14  
376 respectively, Table 2). The δ<sup>18</sup>O of the well waters are -3.0‰ and 0.7‰ and the δD values are -  
377 15‰ for NSHQ04 and 2‰ for NSHQ14. If the dissolved H<sub>2</sub> formed in isotopic equilibrium with  
378 the water, we calculate a temperature of formation of ~50°C using the theoretical  
379 geothermometer developed by Bottinga (1969). The δD values of CH<sub>4</sub> are also low, -205‰ and -  
380 232‰ for NSHQ04\_18m and NSHQ14\_262m, respectively. In contrast, the CH<sub>4</sub> is strongly  
381 enriched in <sup>13</sup>C (δ<sup>13</sup>C CH<sub>4</sub> for NSHQ04\_18m is +2.4‰; NSHQ14\_262m is +3‰) (Table 2).  
382 These δ<sup>13</sup>C CH<sub>4</sub> and δD CH<sub>4</sub> values from Oman subsurface fluids are notably higher than  
383 previously defined isotopic fields for thermogenic, biogenic, and abiotic methane (Figure 2). The  
384 carbonate found in the drill cuttings δ<sup>13</sup>C<sub>VPDB</sub> ranges from -1.48 to -7.05‰ while the δ<sup>18</sup>O<sub>VPDB</sub>  
385 ranges from -7.73 to -11.49‰ (Table 3). The carbonate concentrations in the rock were low and  
386 not quantified.

387 **3.3 Mineralogy of drill cuttings**

388 Bulk powder XRD spectra are similar between the two wells. They are dominated by lizardite  
389 and enstatite and contain magnetite near the surface (Figure 3A,B). In the drill cuttings at 70,  
390 140, and 262m from NSHQ14, there is a brucite peak at  $18.8 2\theta$ , but not at the shallow 17m.  
391 NSHQ04 drill cutting XRD spectra also contain a brucite peak at depth (180 and 303m), but not  
392 at 120m. There is a magnetite peak at  $35.5 2\theta$  in the NSHQ14 drill cuttings at 17 and 70m and in  
393 the NSHQ04 drill cuttings at 120 and 180m.

394  
395 Microscale mineralogical structure and chemistry of drill cuttings were determined by a  
396 combination of petrologic observations, Raman microspectroscopy, Fe K-edge XANES  
397 spectroscopy and electron microprobe analyses. Olivine, diopside, enstatite, chromite, magnetite,  
398 brucite, and two-three different generations of serpentine, both chrysotile and lizardite, were  
399 detected in the drill cuttings of both wells using Raman microspectroscopy (Figure 4). Brucite  
400 and olivine are not detected in the drill cuttings closer to the surface, approximately <120 m. The  
401 NSHQ14 drill cuttings become increasingly serpentinized as they approach the surface, showing  
402 decreasing relict olivine with proximity to the surface and increasing serpentine (Figure 5). The  
403 NSHQ04 drill cuttings also show increased serpentine closer to the surface. There are visually  
404 more pyroxenes present in NSHQ04, both diopside and enstatite (Figure 6), and they appear to  
405 be partially fractured and altered (lower left corner of Figure 5). Drill cuttings from both wells  
406 have magnetite veins and grains ( $\sim 5 \mu\text{m}$ ) between 17-120 meters deep.

407 The Raman maps demonstrate that the drill cutting mineralogy is dominated by two to three  
408 generations of serpentine. Although chrysotile, lizardite, and antigorite can be identified by  
409 Raman spectroscopy from their varying peak positions (Rinaudo et al., 2003; Groppo et al.,  
410 2006; Petriglieri et al., 2015), differences in peak position are relatively small and can be  
411 obscured by large crystal orientation effects on the relative peak intensities. Furthermore, the  
412 effects of varying  $\text{Mg}/(\text{Mg}+\text{Fe})$  and  $\text{Fe}^{3+}/\text{Fe}_T$  on the Raman spectra for the serpentine polytypes  
413 are not yet well quantified. Thus, it is difficult to determine the polymorphs of serpentine with  
414 certainty when just looking at the fingerprint region from  $90\text{-}1600\text{cm}^{-1}$ . By mapping the  
415 serpentine in both the fingerprint region of  $90\text{-}1600\text{cm}^{-1}$  and in the more diagnostic O-H  
416 stretching region of  $3400\text{-}3800\text{cm}^{-1}$ , different regions of serpentine have been identified as  
417 chrysotile and lizardite (Figure 7C).

418 Crosscutting relationships reveal distinct generations of serpentine. NSHQ14 at 262 meters  
419 contains two generations of lizardite with an older lizardite (14-gen1) crosscut by a younger  
420 lizardite (14-gen2) (Figure 4). NSHQ04 at 180 meters has a complex alteration history with a  
421 first generation of chrysotile (04-gen1) overprinted by a younger second generation of chrysotile  
422 (04-gen2). Brucite is intermixed with third generation lizardite (04-gen3). The intermixed  
423 lizardite and brucite are visually apparent in plane polarized light as brown veins (Figure 7). All  
424 depths contain multiple generations of serpentine with chrysotile overprinted by lizardite that is  
425 variably intermixed with brucite. The drill cuttings closer to the surface contain less chrysotile  
426 and more lizardite. There is more brucite at depth than closer to the surface, as evidenced by  
427 powder XRD and Raman spectroscopy. Brucite is visually associated with brown serpentine as  
428 seen in Figure 7.

429 Both NSHQ14 and NSHQ04 drill cuttings contain widespread magnetite (Figure 8) as identified  
430 by Raman microscopy. The magnetite forms both veins and  $2\text{-}10\mu\text{m}$  specks, in some cases in

431 elongate patches or veins cross-cutting all generations of serpentine. Some magnetite is  
432 associated in veins with lizardite, but we can use cross-cutting relationships to infer that some of  
433 the magnetite postdates formation of all other alteration minerals in these drill cuttings. There is  
434 more magnetite observed closer to the surface.

435  
436 The chemical variation between generations of serpentine in well chip NSHQ04\_180m was  
437 quantified with electron microprobe (Table 4). Generations 04gen1 and 04-gen2 chrysotile are  
438 chemically identical and contain high amounts of trace metals, notably an average of 0.67 wt%  
439  $\text{Al}_2\text{O}_3$ , 0.22 wt% MnO and 0.33 weight%  $\text{Cr}_2\text{O}_3$  whereas generation 04-gen3 lizardite has less  
440 than 0.07 wt% of those elements. Generation 04-gen3 lizardite has more MgO (40.90 wt%  
441 versus 36.06 wt%) and less  $\text{SiO}_2$  (34.60 wt% versus 36.87 wt%) than the chrysotile. The totals  
442 are low for the serpentine, possibly due to the presence of brucite intermixed with serpentine as  
443 well as due to structural water.

444 We tried to quantify the amount of brucite and serpentine in the drill cuttings with TGA analysis  
445 (e.g. Lafay et al., 2012). We first measured known amounts of serpentine and brucite separately,  
446 and then mixed the two minerals to verify the method (Supplementary Figure 1). The resulting  
447 spectra and mass estimates are found in supplemental information. From this test, we see that  
448 mixtures of serpentine and brucite are not reliable for determining the mass of both minerals.  
449 Thus, we did not utilize TGA as a technique for quantifying the mass of serpentine and brucite.

#### 450 **3.4 Fe speciation within the drill cuttings**

451 When comparing bulk Fe-XANES of the drill cuttings to the bulk spectra of a partially  
452 serpentinized dunite (OM95-35) from Oman, the drill cutting spectra are more oxidized as noted  
453 by the shift in the spectral features to higher energies (Figure 9). Also, the drill cutting spectra  
454 are more oxidized than San Carlos olivine, the type specimen characteristic of unaltered olivine.  
455 However, it is difficult to discern differences in the Fe-XANES spectra and Fe-speciation (i.e.  
456 average oxidation states and mineralogy) between well depths (Figure 9).

457 The bulk Fe-XANES spectra of the drill cutting samples were fit by Fe XANES model spectra  
458 (e.g. Mayhew et al., 2011) of known minerals in the sample: olivine, pyroxene, brucite,  
459 magnetite, and serpentine. The linear-combination fits to the data show that serpentine increases  
460 in the higher drill cuttings, and olivine and brucite decreases, while pyroxene remains relatively  
461 constant (Supplementary Table 3). The changes in bulk Fe speciation are small and due to the  
462 number of Fe-bearing phases present, the bulk Fe XANES data is relatively insensitive to noted  
463 mineralogical changes such as increased magnetite. We did not collect a highly resolved pre-  
464 edge for the bulk XANES data; thus, it was not possible to quantify a shift in Fe(II)/Fe(III) with  
465 depth.

466 We obtained Fe K-edge  $\mu\text{XANES}$  spectra from the multiple generations of serpentine (as  
467 identified from Raman spectroscopy) to determine variations in Fe-oxidation state and  
468 coordination within serpentines across samples. Three distinct Fe K-edge serpentine spectra with  
469 varying oxidation states are shown in Figure 10. Focusing on the pre-edge (7108-7118eV)  
470 reveals the unoccupied states of the Fe 2p orbital, giving insight into both oxidation state and  
471 coordination (Wilke et al., 2001; Andreani et al., 2013a). The serpentine spectra have a shift in  
472 the centroid position in the pre-edge to higher energy, which reveals that there is a significant  
473 Fe(III) component. In addition, the increase in the fluorescence intensity at higher energy

474 indicates that some of this Fe(III) is tetrahedrally coordinated. The spectra with the prominent  
475 second peak at 7130eV most closely aligns with the lizardite generation identified by Raman,  
476 whereas the most shifted spectrum (prominent peak ~7130

477  
478 .5eV) is associated with the chrysotile. The spectrum most shifted to lower energy is San Carlos  
479 olivine - a reduced spectrum that contains only Fe<sup>2+</sup> (Figure 10). The ferric to ferrous iron ratio  
480 could not be quantitatively calculated using the method of Wilke et al. (2001), Muñoz et al.  
481 (2013), and Andreani et al. (2013a) because these data were collected on a Beamline 2-3 at  
482 SSRL using a Si 110 vs. 311 monochromator, resulting in poorer energy resolution shifts and  
483 broadens the pre-edge features relative to published standards. However, such quantification will  
484 be possible in the future by measuring the same standards across multiple beamlines through  
485 inter-laboratory exchange.

### 486 **3.5 Magnetic hysteresis analysis of the drill cuttings**

487 The drill cuttings exhibit two distinctive types of hysteresis behavior. Drill cuttings deeper than  
488 120m are paramagnetic while those shallower than 120m are ferromagnetic (Table 5). The  
489 ferromagnetic samples (NSHQ14\_17m, NSHQ14\_70m, and NSHQ04\_120m) also show  
490 superparamagnetic behavior, indicating that a population of the magnetic minerals in the samples  
491 are single-domain size particles, likely < 20 nm (Dunlop, 1973; Butler and Banerjee, 1975;  
492 Worm, 1998). We also note a large increase in the saturation magnetization values in the drill  
493 cuttings closer to the surface than at depth in both NSHQ04 and NSHQ14 samples (Table 5).

494 The measured changes in magnetic character augment the petrological observation of increased  
495 magnetite closer to the surface. It is possible to calculate an approximate mass of magnetite in  
496 the sample if we used a proportionality constant of 92 A.m<sup>2</sup>/kg to empirically correlate the  
497 saturation magnetization to the amount of magnetite, as conducted by Malvoisin et al. (2012).  
498 However, such a quantification of magnetite would assume that the sole magnetic carrier in the  
499 sample is magnetite. This assumption may be false in our samples due to the prevalence of  
500 FeII/III-bearing serpentine grains also mixed within the matrix. In addition, the magnetite grains  
501 are present across a large size distribution – both nanoscale and microscale – which affects the  
502 hysteresis parameters that should be applied. For example, we note that the upper drill cuttings  
503 exhibit superparamagnetic behavior, yet the saturation magnetization values used to calculate the  
504 amount of magnetite will only take into account the larger, microscale magnetite grains that  
505 contribute to the non-superparamagnetic components of the data. Thus such a calculation would  
506 be an underestimate of the amount of magnetite present in the drill cuttings; instead, we simply  
507 utilize the suite of magnetic data to show several lines of evidence indicating increased magnetite  
508 formation at shallow depths.

509

### 510 **3.6 16S rRNA analysis of DNA collected from well fluids**

511 We sequenced the hypervariable V4-V5 region of the 16S rRNA gene from DNA extracted from  
512 filters that were loaded with biomass by pumping fluids from each well. Analysis of the 16S  
513 rRNA data shows that the NSHQ14 16S sequences were 99.5% bacteria and 0.05% archaea.  
514 Similar dominance of bacterial sequences was observed in NSHQ04 (99.4% bacteria and 0.06%

515 archaea). The Bacteria are dominated by members of the Deinococcus-Thermus, Nitrospirae,  
516 Firmicutes, Chloroflexi, and Proteobacteria phyla. Fluids from both wells contain candidate  
517 phylum OP1 (1.1 and 2.8%, respectively), and NSHQ04 additionally has candidate phylum OD1.  
518 The species richness, as determined by the number of OTUs from each well, is 1737 for  
519 NSHQ04 fluids vs. 710 for NSHQ14. NSHQ04 is more diverse than NSHQ14.

520 We found that *Meiothermus* (phylum Deinococcus-Thermus, class Deinococci) comprises 8.6%  
521 (NSHQ04) and 46.1% (NSQH14) of the operational taxonomic units (OTUs) in both wells.  
522 *Thermodesulfovibrionaceaea* (phylum Nitrospirae), a sulfate-reducer, comprises 21.6% of  
523 NSHQ14 and 1.4% of NSHQ04. Chloroflexi is prominent in NSHQ04, 5.3%, but only 0.1% in  
524 NSHQ14 (Table 6). Both wells contain Firmicutes (class Clostridia family Anaerobrancaceae),  
525 fermentative microorganisms, and Proteobacteria (genus Hydrogenophaga), hydrogen-oxidizing  
526 bacteria found in other serpentinizing systems (Brazelton et al., 2013; Suzuki et al., 2013). The  
527 fluids from both wells notably contain methanogen *Methanobacterium*, which can utilize  
528 hydrogen and variable carbon sources such as formate to produce methane. *Methylococcus*, a  
529 methanotroph, is also present.

530 **4. Discussion**

531 This study explores the mineralogy and aqueous geochemistry of modern water/rock reactions  
532 associated with low temperature serpentinization and hydrogen production in Oman and how  
533 these processes may give rise to habitable conditions for microbial life in the peridotite aquifer.  
534 We then use 16S rRNA sequencing of DNA extracted from subsurface fluids to investigate the  
535 phylogenetic diversity of the fluid microbial communities and infer potential microbial  
536 metabolisms sustained in-situ.

537 **4.1 Fluid chemistry of low temperature serpentinization**

538 Modern alteration of primary minerals in the aquifer is evident from the abundant  $\text{Ca}^{2+}$  and  $\text{OH}^-$   
539 in peridotite hosted well waters NSHQ04 and NSHQ14 (Neal and Stanger, 1983; Neal and  
540 Stanger, 1984; Neal and Stanger, 1985). Neal and Stanger (1983, 1984, 1985) extensively studied  
541 the hydrogeology of Oman's fluids and coined these hyperalkaline waters ( $\text{pH} > 11$ ) containing  
542  $\text{Ca}^{2+}$ - $2\text{OH}^-$  as Type II fluids, following the initial observation of Barnes and O'Neil (1969). They  
543 are situated in serpentinized dunite and harzburgite and are derived from serpentinization  
544 reactions with subsurface fluids that are isolated from the atmosphere. The hydration of olivine  
545 and pyroxene causes the water to become enriched in  $\text{Ca}^{2+}$ - $\text{OH}^-$  (Barnes and O'Neil, 1969; Neal  
546 and Stanger, 1984; Bruni et al., 2002; Kelemen et al., 2011):

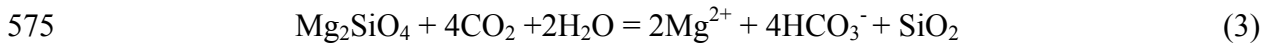


550 The  $\text{Ca}^{2+}$  is released from diopside (present in all drill cuttings), and then accumulates in the  
551 water because  $\text{Ca}^{2+}$  is not incorporated into serpentine minerals (Barnes et al., 1967). These Type  
552 II fluids are carbon-depleted and when they emerge at surface springs, they rapidly mix with  
553 atmospheric carbon dioxide to precipitate carbonate minerals (Stanger, 1986; Kelemen and  
554 Matter, 2008; Kelemen et al., 2011; Paukert et al., 2012; Mervine et al., 2014). The  $\text{Ca}^{2+}$  values  
555 we measure in the deeper subsurface fluids are  $\sim 1\text{mM}$  higher than those reported from  
556 hyperalkaline springs, presumably because  $\text{Ca}^{2+}$  in the subsurface has not been depleted through  
557 the precipitation of carbonate minerals. Thus, sampling the Type II fluids in wells before they  
558 interact with atmospheric  $\text{CO}_2$  in the unsaturated zone or on the surface provides a more direct  
559 assessment of the water composition in the aquifer.

560  
561 The subsurface well water contains more  $\text{Cl}^-$  than found in Oman rainwater and hyperalkaline  
562 surface seeps (Paukert et al., 2012) which provides additional proof that modern water/rock  
563 interaction is occurring. We infer that the high  $\text{Cl}^-$  concentrations are due to the presence of  $\text{Cl}^-$   
564 that was incorporated in the Oman peridotite during initial, high-temperature serpentinization  
565 near an oceanic spreading ridge, and dissolved in groundwater during ongoing weathering  
566 (Stanger, 1986). The  $\text{Cl}^-$  is presumably at lower concentrations at the surface seeps than in the  
567 wells because it is precipitating with carbonates in salt.

568 The wells only contain Type II fluids; however, the shallow peridotite aquifer in Oman also hosts  
569  $\text{Mg}^{2+}$ - $2\text{HCO}_3^-$  as observed by Barnes and O'Neil (1969). These are termed Type I fluids (Neal  
570 and Stanger, 1983; Kelemen et al., 2011) and are moderately alkaline fluids of a  $\text{Mg}^{2+}$ - $2\text{HCO}_3^-$   
571 composition found in the shallow groundwater ( $\sim \text{pH} 8-9$ ). In Oman, Type I fluids are typically  
572 found in wadi (channel that is dry except during rainy seasons) pools, ultramafic wadi gravels,

573 and water wells (e.g., Neal and Stanger, 1985; Paukert et al., 2012) and form through the  
574 following simplified reaction (e.g. Kelemen et al., 2011):



576 Atmospheric carbon dioxide dissolves in the water and forms bicarbonate as olivine and  
577 serpentine minerals in the near-surface react with the waters and release magnesium ions and  
578 silica. Although we did not observe Type I fluids in this study, their mixing and interaction with  
579 Type II fluids may be influencing water/rock reactions and microbial diversity in the subsurface.  
580 In particular, the presence of oxygenated Type I fluids in the highly fractured upper portion of  
581 the aquifer may explain the aerobic organisms detected by 16S rRNA sequencing.

582

#### 583 *4.2 Mineral assemblages associated with low temperature hydrogen production*

584

585 We investigated the mineralogy of the subsurface aquifer to see if the mineral assemblages give  
586 insight into the water/rock reactions and mechanisms that produce hydrogen at low-temperature.  
587 The drill cuttings contain serpentine, brucite, and magnetite, as is common in partially  
588 serpentinized peridotites. Although the drill cuttings are heavily serpentinized, they still contain  
589 relict olivine at depth that diminishes towards the surface, which suggests olivine may be the  
590 dominant mineral reacting with the in-situ fluids. There is a significant portion of unaltered  
591 pyroxene that could also be reacting; however, few zones of pyroxene alteration have been  
592 observed. Pyroxene alteration can be a dominant reaction in other serpentinizing sites (Klein et  
593 al., 2009; Marcaillou et al., 2011; Andreani et al., 2013a). A common alteration product of  
594 pyroxene is talc [ $\text{Mg}_3\text{Si}_4\text{O}_{10}(\text{OH})_2$ ] under conditions of high silica activity (Frost and Beard,  
595 2007; McCollom and Bach, 2009; Klein et al., 2013). We do not observe any talc formation;  
596 thus, we do not believe pyroxene alteration is dominating the water/rock reactions, although the  
597 high concentrations of  $\text{Ca}^{2+}$  in the fluids do suggest that at least some pyroxene dissolution is  
598 occurring in the hyperalkaline aquifer.

599 The multiple generations of serpentine observed in the drill cuttings reveal that the mantle  
600 peridotite experienced multiple periods of water/rock alteration. The mantle section of the  
601 ophiolite was first serpentinized near an oceanic spreading ridge, during emplacement of the  
602 ophiolite onto the Arabian continental margin, and/or during subaerial erosion and a subsequent  
603 marine transgression in the late Cretaceous (Kelemen and Matter, 2008; Hanghøj et al., 2010;  
604 Mervine et al., 2014). These events may have caused formation of the extensive chrysotile  
605 matrix seen in the drill cuttings. The chrysotile is overprinted by lizardite veins; however, we  
606 cannot infer a formation temperature due to the fact that chrysotile is metastable relative to  
607 lizardite (Evans, 2004).

608 We characterized the Fe content and speciation of the serpentine to investigate reservoirs of Fe in  
609 the system. Both the lizardite and chrysotile contain ~7-8 wt.%  $\text{FeO}_T$  (considering all Fe as  $\text{Fe}^{2+}$ ).  
610 In average natural samples, chrysotile contains 3 wt.%  $\text{FeO}_T$ , while lizardite ranges from 2-8  
611 mol.% Fe (Evans et al., 2009; Streit et al., 2012). Thus, the chrysotile in Oman is Fe-rich while  
612 the lizardite is average. Characterization of serpentine in our samples with electron microprobe  
613 and XANES confirms the presence both Fe(II) and Fe(III) in the serpentine. Fe(III) can  
614 substitute into both the octahedral and tetrahedral sites, replacing  $\text{Si}^{4+}$ , to form cronstedtite,  
615  $(\text{Mg}_2, \text{Fe}^{3+})_3(\text{Fe}^{3+}, \text{Si})_2 \text{O}_5(\text{OH})_4$  (Frost and Beard, 2007; Klein et al., 2009; Evans, 2010; Streit et  
616 al., 2012). The formula for chrysotile inferred during early alteration of the peridotite is





662 Brucite can accommodate Fe(II) in its structure that can then be oxidized during subsequent  
663 alteration to produce hydrogen at low temperatures (Klein et al., 2013). Typically, brucite forms  
664 mesh rims around olivine and traps Fe(II) in a stable mineral structure and prevents hydrogen  
665 generation (Klein et al., 2009; Evans, 2010). However, in our drill cutting samples, and in our  
666 comparison Oman dunite sample, we observe brucite intimately intermixed with lizardite. It is  
667 not possible to determine an iron content for the brucite due to the fact that it is not present in  
668 large enough, serpentine-free areas for analysis. Electron microprobe measurements were not  
669 used to constrain Fe-contents of brucite intermixed with serpentine because Fe can substitute into  
670 Si sites in serpentine (particularly in Fe(III) rich serpentine) as well as Mg sites in brucite, thus  
671 an estimate of brucite calculated from electron microprobe would be inaccurate. However,  
672 Raman analysis shows a distinct change in the brucite spectrum from that of the pure Mg(OH)<sub>2</sub>  
673 endmember. Additionally, brucite in serpentinizing systems commonly contains iron; brucite can  
674 include greater than 10 wt% FeO<sub>T</sub>, with increasing Fe content at lower temperatures in the same  
675 bulk composition (Moody, 1976; Klein et al., 2009). Yet brucite is not thermodynamically stable  
676 at the silica activities measured in our fluid samples (Table 1). Thus, we propose that brucite  
677 should react with silica-rich fluids in the aquifer (Bach et al., 2006), driving Fe(II) to undergo  
678 oxidation to form Fe(III)-rich serpentine and/or magnetite while concurrently reducing H<sub>2</sub>O to  
679 make H<sub>2</sub> (see equation 7 below).

680  
681 There are several possible reasons for the high silica activity in our fluid samples. First, the fluids  
682 in the wells are high in Ca<sup>2+</sup>. Well NSHQ04 is close to the Moho, the zone of contact between  
683 peridotite and gabbro. Thus, it is possible gabbro-equilibrated fluids are interacting with the  
684 peridotite aquifer. Fluid that has equilibrated with gabbro has higher silica activity, and it will  
685 destabilize and consume brucite (Frost and Beard, 2007). However, there is insufficient  
686 hydrological information about the region surrounding the wells to test this hypothesis, and the  
687 similarity of fluids in wells NSHQ04 (near the Moho) and NSHQ14 (kilometers from the Moho)  
688 seems inconsistent with this hypothesis.

689  
690 Bach et al. (2006) suggest that high Si fluids are generated when olivine nears exhaustion in the  
691 host rock and pyroxene alteration becomes a more important control on fluid chemistry. This is  
692 plausible given the low amount of relict olivine remaining in the drill cuttings.

693  
694 A third possibility, as shown in equation 3, is that the generation of Type I waters in the shorter  
695 residence fluid-flow pathways can lead to fluids with high silica activities. Subsequently, we  
696 may be observing the destabilization of brucite in the host rock when Type I waters mix with  
697 Type II fluids within the shallow subsurface. This is supported by the observation of decreasing  
698 brucite in the highly serpentinized samples near the surface where Type I waters may be present.

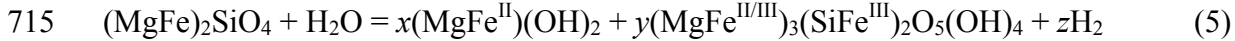
699  
700 There is increased extent of serpentinization in the drill cuttings near the surface as opposed to at  
701 depth, which suggests varying hydrological pathways in the subsurface. The top tens of meters  
702 below the surface could be subject to more variable conditions with higher water/rock ratios  
703 and/or interaction with Type I fluids than rock at depth due to rainwater recharge. This can lead  
704 to increased fracture permeability (e.g., Kelemen and Hirth, 2012) and periodic exposure to  
705 oxygen, as well as shorter fluid residence times. Thus, the fluids will not be equilibrated with the  
706 mineral assemblages, leading to more rapid destabilization and alteration, as well as increased  
707 oxidation and drive to form magnetite.

708

### 709 4.3 Hydrogen generating reactions

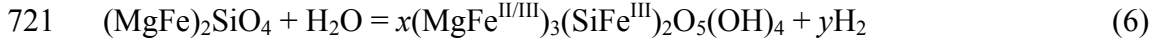
710

711 Based on our observations, we infer that three different hydrogen generating reactions have  
712 occurred in the subsurface. An initial serpentinization stage prior to modern water/rock reactions  
713 produced hydrogen from alteration of olivine and led to the production of Fe(II)-bearing brucite  
714 and Fe(III) rich serpentine (chrysotile generation):



716 There is relict olivine in the deep drill cuttings that is replaced by serpentine at shallower depths,  
717 so similar H<sub>2</sub> generating reactions could occur today. Moreover, less brucite might form because  
718 modern silica activities in the fluids are too high for brucite stability. Thus we suggest that relict  
719 olivine is now reacting to form new Fe(III)-bearing lizardite and hydrogen at low temperatures:

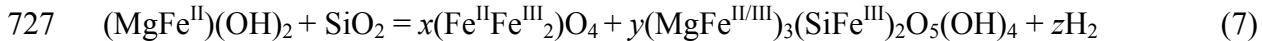
720



722

723 Currently, a high silica fluid is interacting with the rock, destabilizing the Fe(II)-bearing brucite  
724 (as modeled in Geochemist Workbench). This leads to the formation of magnetite and lizardite,  
725 with the production of hydrogen:

726



728 The destabilization of Fe(II)-bearing brucite to form magnetite and serpentine, and the alteration  
729 of olivine to Fe(III) rich serpentine, should both produce hydrogen at low temperatures. This  
730 model of alteration and hydrogen generation is consistent with observations by Andreani et al.  
731 (2013b) that serpentinites from mid-ocean ridges contain both Fe(III)-serpentine and more  
732 magnetite as the degree of serpentinization increases.

733

### 734 4.4 Isotopic signature of hydrogen and methane

735

736 The isotopic signature of the H<sub>2</sub> serves as a valuable indicator of formation temperature, which  
737 complements mineralogical observations of serpentinization leading to hydrogen production.  
738 (Neal and Stanger, 1983) collected gas samples from surface hyperalkaline seeps and observed  
739 low δD H<sub>2</sub> values (-697‰ and -714‰) similar to those measured from our well samples (-680‰  
740 and -686‰). They noted that H<sub>2</sub>- and CH<sub>4</sub>-rich gases (H<sub>2</sub> as high as 99% and CH<sub>4</sub> as high as  
741 4.3%) emerge at hyperalkaline surface seeps, whereas the well fluids provide access to dissolved  
742 gases in the host rock itself. Sherwood Lollar et al. (1993), Proskurowski et al. (2006), and  
743 Abrajano et al. (1990) also found negative δD gases that formed at low temperatures (<200°C) at  
744 other serpentinizing sites (both continental and oceanic), as shown in Table 4.

745

746 The dissolved gases from Oman subsurface wells uniformly contain some of the most negative  
747 δD hydrogen gas found in nature. We calculate a formation temperature of ~50°C by applying  
748 the geothermometer of Bottinga (1969) to the coupled δD H<sub>2</sub> and δD H<sub>2</sub>O in the well fluids.  
749 Assuming the geothermal gradient at NSHQ14 is approximately 25°C/km (Paukert et al., 2012),  
750 the gases are hypothesized to form at a depth of less than 2km. A formation temperature of

751 ~50°C supports the hypothesis that low-temperature serpentinization and hydrogen formation is  
752 occurring in the Oman aquifer, rather than H<sub>2</sub> being physically released from hydrogen  
753 inclusions that formed during higher temperature serpentinization events (McCollom and  
754 Seewald, 2001). We verified the lack of gas-rich inclusions in relict olivine by extensively  
755 probing the olivine grains by confocal Raman spectroscopy. However, the mantle section of the  
756 ophiolite is up to 8 km thick (Ravaut et al., 1997); thus, the H<sub>2</sub> could be generated at  
757 temperatures as high as 200°C and then migrate upwards to the surface. In this case, the current  
758 negative δD of the H<sub>2</sub> could instead represent isotopic exchange and re-equilibration between the  
759 H<sub>2</sub> and H<sub>2</sub>O after formation of the H<sub>2</sub> as the waters circulate to shallower, cooler depths.

760 NSHQ04 fluids contain millimolar amounts of CH<sub>4</sub>, which may be produced abiotically due to  
761 the highly reducing conditions reflected in the abundant H<sub>2</sub> in the system. In olivine dissolution  
762 reactions at 30+°C, (Neubeck et al., 2011) observed measurable CH<sub>4</sub>, potentially through the  
763 oxidation of H<sub>2</sub> and reduction of CO<sub>2</sub> (Sleep et al., 2004). However, the CH<sub>4</sub> detected by  
764 Neubeck et al. (2011) could have been released from fluid inclusions, or produced by reaction of  
765 fluid with the experimental reaction vessel. At higher temperature (>120°C), CH<sub>4</sub> production can  
766 occur abiotically through Fischer-Tropsch-type or Sabatier reactions, through catalysis by  
767 magnetite and awaruite (Ni-Fe alloy) commonly found in serpentinites (Frost, 1985; Lorand,  
768 1987; Horita and Berndt, 1999). Etiope et al. (2013) suggested catalysts such as ruthenium or  
769 chromite produce methane at temperatures <50°C. Such low temperature methane production  
770 may be possible in Oman due to the abundance of magnetite, chromite and awaruite found in the  
771 partially serpentinized mantle peridotites. Alternatively, methane formation could be biologically  
772 mediated by methanogens.

773  
774 The δ<sup>13</sup>C CH<sub>4</sub> signatures are the highest values reported in the literature thus far despite the wide  
775 range of methane isotopic compositions compiled in the past 30+ years. Plots comparing the  
776 ranges of δ<sup>13</sup>C CH<sub>4</sub> and δD CH<sub>4</sub> found in various geologic environments (Whiticar, 1990; Etiope  
777 et al., 2013) give context to methane isotopic compositions measured in the peridotite-hosted  
778 wells in Oman. Thermogenic natural gas has been extensively studied, as have gases from  
779 extreme environments like hyperalkaline lakes and Antarctic ice sheets (Whiticar, 1990). The  
780 previously highest documented δ<sup>13</sup>C CH<sub>4</sub> values (-1.6‰) were found from the Ilimaussaq  
781 inclusions Greenland (Laier and Nytoft, 2012; Etiope et al., 2013). That methane was  
782 hypothesized to have a biological origin, and subsequent sediment burial and partial loss by  
783 diffusion during uplift and erosion enriched the gas in isotopically heavy methane (Laier and  
784 Nytoft, 2012). A similar explanation is plausible for the enriched δ<sup>13</sup>C CH<sub>4</sub> values in Oman.  
785 Alternatively, if the methane we observe in Oman formed abiotically at 50°C at a depth of ~2km,  
786 similar to the H<sub>2</sub>, slow diffusion upwards from depth could fractionate and enrich the remaining  
787 methane in isotopically heavy carbon after the lighter <sup>12</sup>C CH<sub>4</sub> has diffused away. However, this  
788 should have a similar effect on the hydrogen isotopic composition of the methane as well, which  
789 we did not observe. The methane-hydrogen D/H fractionation can be used to estimate  
790 temperature of formation of methane (Horibe and Craig, 1995) at ~70° +/- 3°C.

791 The isotopic composition of methane collected from wells in Oman falls near the traditionally  
792 defined abiotic range. Abiotic methane tends to have δ<sup>13</sup>C CH<sub>4</sub> values greater than -50‰ and δD  
793 of CH<sub>4</sub> can range from -450 to -50‰ (Etiope and Sherwood Lollar, 2013; Etiope et al., 2013).  
794 Bacterial reduction of CO<sub>2</sub> to methane gives negative δ<sup>13</sup>C CH<sub>4</sub> values as low as -110‰ and δD

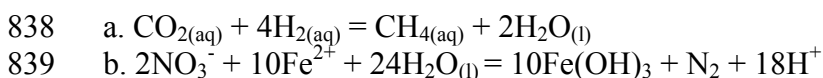
795 CH<sub>4</sub> down to -531‰ (Whiticar, 1999); thus, methane from Oman does not have a traditional  
796 bacterial signature. Low temperature CH<sub>4</sub> production has been experimentally demonstrated with  
797 ruthenium and rhodium catalysts (Jacquemin et al., 2010). Platinum group metal inclusions,  
798 including Ru and Rh, are found in chromites (e.g, Jacquemin et al., 2010). Platinum group metals  
799 in chromites in Oman could be catalyzing low temperature methane formation and leading to a  
800 heavy δ<sup>13</sup>C CH<sub>4</sub> signature, but there are no experimental data to confirm this hypothesis. δ<sup>13</sup>C  
801 enriched CH<sub>4</sub> can also be produced by extensive biological oxidation of biogenic or abiogenic  
802 methane that enriches the residual methane in <sup>13</sup>C (Whiticar and Faber, 1986; Whiticar, 1999).  
803 Thus, if methane cycling is active in the subsurface aquifer, the isotopic signature of CH<sub>4</sub> may  
804 not be an unequivocal marker of the methane formation pathway (Whiticar and Faber, 1986;  
805 Templeton et al., 2006).

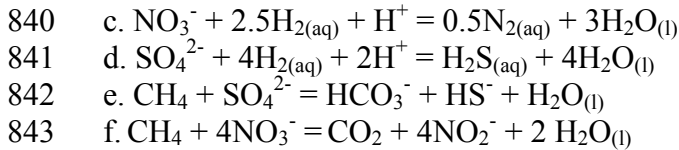
806 The processes giving rise to the heavy δ<sup>13</sup>C CH<sub>4</sub> in Oman cannot be elucidated without further  
807 investigation of the microbial and low-temperature abiotic pathways that are giving rise to the  
808 production of mM concentrations of CH<sub>4</sub>. First, the source of carbon must be assessed. The δ<sup>13</sup>C  
809 signature of carbonates mineralized in Oman peridotites provide some insights into the isotopic  
810 signature of the carbon pool. The carbonate found in the drill cuttings δ<sup>13</sup>C ranges from -1.48 to -  
811 7.05‰ while the δ<sup>18</sup>O is -7.73 to -11.49‰. These values are similar to the Mg-rich carbonate  
812 veins from outcrops and roadcuts that have δ<sup>13</sup>C ranging from -25.98 to 0.98‰ and δ<sup>18</sup>O from -  
813 7.04 to 5.56‰ (Clark and Fontes, 1990; Kelemen and Matter, 2008; Kelemen et al., 2011;  
814 Mervine et al., 2014). The negative δ<sup>13</sup>C values as low as -26‰ probably formed through a  
815 mechanism dominated by kinetic isotope fractionation during carbonate precipitation. Both the  
816 values from the drill cuttings and outcrops are still lighter than δ<sup>13</sup>C in the CH<sub>4</sub>, suggesting that  
817 even if the entire DIC pool was converted to methane under extreme carbon limitation, processes  
818 such as further δ<sup>13</sup>C enrichment by diffusion or partial oxidation of the methane must be  
819 invoked.

#### 821 *4.5 Potential metabolic pathways supported by hyperalkaline fluids*

822  
823 The hyperalkaline fluids in Oman contain electron donors and acceptors to sustain anaerobic  
824 microbial metabolisms. There are millimolar amounts of H<sub>2</sub> and CH<sub>4</sub> to serve as electron donors,  
825 but dissolved organic acids were not detected at the micromolar detection limit. NSHQ04  
826 notably contains high levels of SO<sub>4</sub><sup>2-</sup>, which may be a source of critical electron acceptors for  
827 microorganisms (ex. sulfate reducers). Nitrate found in both wells is another potential electron  
828 acceptor that can be coupled with oxidation of H<sub>2</sub>, CH<sub>4</sub> and Fe(II).

829  
830 The aqueous geochemistry of the well fluids can support several potential metabolic pathways.  
831 Well fluids contain more sulfate and nitrate than samples from hyperalkaline seeps with  
832 comparable pH, and elevated H<sub>2</sub> and CH<sub>4</sub> (Paukert et al., 2012). Thus, nitrate and sulfate  
833 reduction at depth, tied to hydrogen oxidation, is likely. The high methane concentrations in  
834 NSHQ04 can support anaerobic oxidation of methane (AOM) (Hoehler et al., 1994; Joye et al.,  
835 2004), especially considering AOM consortia are often syntrophically associated with sulfate-  
836 reducing microorganisms. The following reactions are often invoked for serpentinizing systems  
837 and may be relevant metabolisms for microbial life in the subsurface of Oman:





844  
845 (Hoehler et al., 1994; Nielsen and Nielsen, 1998; Chapelle et al., 2002; Cardace and Hoehler,  
846 2009; Haroon et al., 2013; Cardace et al., 2015). These metabolic strategies provide the energy to  
847 generate an electrochemical gradient to produce ATP. However, it is energetically taxing to  
848 generate a traditional hydrogen pump at high pH (Hicks et al., 2010; Suzuki et al., 2014).  
849 Microorganisms in Oman may be employing a sodium or calcium motive force to generate ATP  
850 instead of a proton pump. Many microorganisms pump  $\text{H}^+$  ions outside the cell to create an  
851 energy gradient, but in a high pH environment, this  $\text{H}^+$  quickly combines with abundant  $\text{OH}^-$  in  
852 the environment and cannot be utilized by the cell. Microorganisms can adapt to hyperalkaline  
853 conditions by generating a sodium motive force instead of pumping protons onto the surface of a  
854 cell inundated with  $\text{OH}^-$ . There is ample  $\text{Na}^+$  in the fluids, so organisms in Oman may use a  
855 sodium motive force to cope with high pH environments. Alternatively, recent work has shown  
856 that some organisms can utilize a proton motive force, even under alkaline conditions  
857 (Mulkidjanian et al., 2008; Hicks et al., 2010; Suzuki et al., 2014). The pH in NSHQ04 is slightly  
858 lower than in NSHQ14, potentially making it more habitable for microorganisms. NSHQ04 also  
859 has more abundant electron donors, nitrate and sulfate, than NSHQ14, further increasing its  
860 habitability.

#### 861 862 **4.6 Organisms detected in fluids from 16S rRNA sequencing** 863

864 Predictions about potential metabolic pathways in serpentinizing systems aid in interpreting 16S  
865 rRNA data from the fluids and allow us to place the phylogeny of the organisms detected in the  
866 subsurface fluids within a context of potential functional activities. There is a curious mixture of  
867 both aerobic and strictly anaerobic microorganisms in the subsurface. DNA extracted from well  
868 fluids shows the presence of aerobic organisms *Meiothermus* and *Hydrogenophaga* that require  
869 oxygen as an electron acceptor. *Meiothermus* is considered to be obligately aerobic and  
870 chemoorganotrophic, capable of utilizing a range of carbon sources from glucose to acetate  
871 (Tindall et al., 2010). *Hydrogenophaga* is chemoorganotrophic or chemolithoautotrophic, and it  
872 oxidizes hydrogen and reduces organic material or heterotrophically denitrifies nitrate (Willems  
873 et al., 1989). We also found members of the Clostridia class and *Methanobacterium* genera,  
874 which are strict anaerobic fermenters and methanogens, respectively. Anaerobes  
875 *Thermodesulfobivibrionaceae* are also present, which are sulfate reducing bacteria that use  
876 hydrogen as electron donors and ferment pyruvate or other organics (Haouari et al., 2008). We  
877 likely significantly mixed the deep and shallow well fluids during pumping, so there may be  
878 internal variation in the fluid Eh as a function of depth, and intervals of variable permeability,  
879 that affect microbial community composition and function in ways that we cannot yet identify.  
880 The near-surface fluids probably have a shorter residence time and more recent interaction with  
881 ambient atmospheric oxygen. The mixture of organisms may point to an upper zone of more  
882 oxidized fluids in the wells (e.g. Type I fluids), leading to an interesting geochemical interfaces  
883 that microorganisms can exploit.

884 *Methanobacterium*, a methanogen, is present in NSHQ04 and NSHQ14. This may explain the  
885 abundant  $\text{CH}_4$  in the wells. It is a strict anaerobe that oxidizes  $\text{H}_2$  and reduces formate,  $\text{CO}$ , or

886 CO<sub>2</sub> to produce methane (Balch et al., 1979). Similar *Methanobacterium* sequences have also  
887 been observed in the Zambales ophiolite seeps (Woycheese et al., 2015). Methanogenesis is  
888 oftentimes invoked as a metabolic pathway in serpentinizing environments due to the abundant  
889 hydrogen and methane in the fluids (Chapelle et al., 2002; Cardace and Hoehler, 2009; Cardace  
890 et al., 2015). In order to determine *Methanobacterium*'s contribution to the CH<sub>4</sub> in the wells, it  
891 will be necessary to investigate the abundance and activity of the methanogens along with the  
892 isotopic signature of the CH<sub>4</sub> that they produce.

893 Candidate phylum OP1 was first detected in hot springs, but curiously it is present in the  
894 mesophilic, hyperalkaline conditions of the Oman subsurface. OP1 was first found in a neutral  
895 hot spring (75-95°C) in Yellowstone rich in iron, sulfide, carbon dioxide, and hydrogen (Kumar  
896 and Saravanan, 2011). There is a nearly complete genome for the OP1 *Candidatus*  
897 '*Acetothermus autotrophicum*' that suggests it is one of the earliest bacteria to branch from the  
898 last universal common ancestor (Takami et al., 2012). 13 of the OTUs from NSHQ14 have 100%  
899 identity to this genome, whereas the other 250 OTUs are other species from candidate phylum  
900 OP1. The genome for *Candidatus* '*Acetothermus autotrophicum*' has a high GC content (61.9%),  
901 and this organism is estimated to have an ideal growth temperature of 84.7°C. It also is  
902 phylogenetically similar to the members of the Deinococcus-Thermus clade, which is interesting  
903 giving the high concentrations of *Meiothermus*, a similar genera, in the wells. The proposed  
904 metabolism of '*A. autotrophicum*' is acetogenesis through the acetyl CoA pathway utilizing CO<sub>2</sub>  
905 and H<sub>2</sub>, which is an ancient C-fixation pathway (Takami et al., 2012). Candidate phyla by  
906 definition are phyla with no cultured and formally described representative strains, so little to  
907 nothing is known about their metabolic requirements and physiology. Future microbiological  
908 studies of Oman subsurface fluids may provide more insight into the function of these  
909 organisms, particularly if they can be cultured and studied in the laboratory.

910 A diverse range of phyla were identified from the well fluids. Clostridia and *Hydrogenophaga*  
911 are abundant in the fluids, supporting the idea that previous studies probing hyperalkaline seeps  
912 were identifying organisms that are indeed present in the subsurface (Brazelton et al., 2013;  
913 Suzuki et al., 2013). The *Hydrogenophaga* sequences detected here were 100% identical to  
914 *Serpentinomonas* (Suzuki et al., 2014), a bacterium cultured and characterized from the Cedars  
915 ophiolite. This organism is an obligate alkaliphile with an optimum growth pH of 11. It utilizes  
916 H<sub>2</sub>, CaCO<sub>3</sub>, and O<sub>2</sub> for growth. Clostridia, specifically members of the *Erysipelothrix* group,  
917 found in these samples were also found in the Tablelands Ophiolite, and this group is known to  
918 contain abundant fermentation-associated hydrogenases, suggesting that it uses organic  
919 compounds to survive (Brazelton et al., 2013). Lipids extracted from brucite-calcite veins at the  
920 Iberia margin, a Lost-City type hydrothermal field, are also hypothesized to correspond to  
921 *Desulfotomaculum* and *Clostridium* (Klein et al., 2015); thus, Clostridia are widespread in  
922 serpentinizing systems. Additionally, these anaerobic organisms contain [FeFe]-hydrogenases  
923 that can catalyze hydrogen production from the reduction of organic materials like acetate and  
924 formate (Brazelton et al., 2012). Clostridia are also endospore-forming, which may allow them to  
925 persist in these fluids during nutrient-poor periods (Madigan, 2012).

926 The metabolic pathways of the 16S rRNA correspond to predictions of potential metabolisms in  
927 the fluids that are derived from the in-situ geochemistry. Chloroflexi have a range of metabolic  
928 strategies which include fermentation, CO<sub>2</sub> fixation, and acetogenesis (Hug et al., 2013).  
929 *Thermodesulfovibrionaceae* is a sulfate-reducer, and some species of Clostridia may also be

930 capable of sulfate reduction (Madigan, 2012). There are several Gammaproteobacteria in the  
931 fluids that may be denitrifiers (e.g. the extensively studied *Psuedomonas stutzeri*) (Madigan,  
932 2012). The other predicted metabolisms, such as methane oxidation and sulfate reduction, may  
933 be facilitated by Methylococcales and Desulfovibrionales.

934 The two wells host different microbial communities. This is most likely dictated by the varying  
935 geochemistry and pH between the subsurface systems. NSHQ04 has a lower pH (10.5) and more  
936 electron acceptors such as nitrate and sulfate to make it more habitable and diverse. NSHQ04  
937 also has higher concentrations of CH<sub>4</sub> than NSHQ14, which is reflected in the fact it contains  
938 methane oxidizers. Although our method of 16S rRNA amplicon sequencing does not reflect the  
939 quantity of organisms in the system, it does reveal that geochemistry strongly modulates  
940 microbial ecology in hyperalkaline subsurface fluids.

#### 941 4.7 Carbon sources in hyperalkaline fluids

942 The well fluids from 2012 are carbon-poor with DIC concentrations that vary from 0.078-  
943 0.391mM. It is possible that the highly reducing conditions produced by high levels of H<sub>2</sub> in  
944 serpentinizing environments lead to the abiogenic formation of low weight molecular acids  
945 (Lang et al., 2010; Schrenk et al., 2013). McCollom and Seewald (2001) observed formation of  
946 formate during 300°C olivine serpentinization experiments:



948 High concentrations of formate (36-158 µm/kg) are observed at the Lost City Hydrothermal  
949 Field, and isotopic data suggest that the formate formed abiotically (Proskurowski et al., 2006;  
950 Lang et al., 2010). However, low molecular weight organic acids were not detected above the  
951 micromolar detection limit for the species measured in our samples, suggesting that they are not  
952 extensively produced under in-situ conditions. Alternatively, the absence of formate and other  
953 organic acids could be due to their rapid consumption by subsurface microorganisms.

954 We searched for complex organic carbon in the Oman drill cuttings as a potential carbon source  
955 and indicator of microbial life, but no accumulations of macromolecular carbon were detected in  
956 the well chips by Raman spectroscopy. Raman spectroscopic mapping has successfully been  
957 used to search for signs of life within serpentinized peridotites from the Mid-Atlantic Ridge,  
958 where complex organic carbon has been found in association with cavities in hydroandraditic  
959 garnets (Ménez et al., 2012). These hollow cavities are thought to host cryptoendolithic  
960 microbes, metabolizing H<sub>2</sub> generated through serpentinization or using Fe(III) in garnets as an  
961 oxidant for H<sub>2</sub>. Complex organic molecules from these organisms might then migrate into the  
962 surrounding serpentines and ocean, providing a source of carbon for other microbial life (Pasini  
963 et al., 2013).

964  
965 We also measured total organic carbon (TOC) in the drill cuttings through combustion  
966 techniques, but the results are likely overestimates because residual magnesite may be present  
967 (Supplementary Table 1). Organic carbon could derive from a rock-hosted biome, but these  
968 concentrations of organic carbon could also be a relic of drilling contamination or abiotic  
969 reduction of CO<sub>2</sub>. Further information about molecular structure and distribution of organic  
970 carbon are necessary to characterize its source.

971



972 Heavily altered Oman peridotites contain extensive carbonate vein networks (Kelemen and  
973 Matter, 2008; Kelemen et al., 2011; Streit et al., 2012; Paukert et al., 2012; Mervine et al., 2014)  
974 which may provide an unconventional carbon source to microorganisms in the subsurface.  
975 Previous work by Suzuki et al. (2014) shows the *Serpentinomonas* can utilize  $\text{CaCO}_3$  as a carbon  
976 source. However, we do not detect the presence of carbonate veins in the drill cuttings, but they  
977 are most likely a small component (aqueous carbonic acid was not measured) so would not be  
978 easily detected by bulk powder XRD. We did a simple test for carbonate by adding HCl and  
979 measuring change in mass and observe about 1% carbonate in the drill cuttings; this is also a low  
980 estimate, since the analysis is neglecting to measure magnesite. Thus, carbonate veins in the  
981 rocks may be a carbon source for organisms in the subsurface.

982 Finally, Type I, Mg- $\text{HCO}_3$ -rich waters are abundant in Oman, and contain 1-10 mM total carbon  
983 (e.g., compiled data in Supplement of Kelemen and Matter, 2008). Type I waters could supply  
984 carbon for growth of micro-organisms by infiltration into more heavily reacted rocks hosting  
985 Type II waters.

986 **5. Conclusions**

987 Subsurface mantle peridotites from the Samail Ophiolite in Oman are highly serpentinized and  
988 oxidized, and are in contact with hyperalkaline (>pH 10) fluids high in  $\text{Ca}^{2+}$ ,  $\text{OH}^-$ , dissolved  $\text{H}_2$   
989 and  $\text{CH}_4$ . High concentrations of very negative  $\delta\text{D}$   $\text{H}_2$  values are inferred to have formed or  
990 equilibrated at  $\sim 50^\circ\text{C}$ . The coupled  $\delta\text{D}$  and positive  $\delta^{13}\text{C}$  of the dissolved  $\text{CH}_4$  would  
991 traditionally be interpreted as abiotic, and dissolved  $\text{CH}_4$  has the most isotopically heavy  $\delta^{13}\text{C}$   
992  $\text{CH}_4$  reported in the literature thus far. We suggest that the methane isotopic signature is in part  
993 modulated by significant oxidation, whether it was produced through biotic or abiotic pathways.

994 We hypothesize that these gas-rich hyperalkaline fluids have evolved through an ongoing stage  
995 of low temperature serpentinization in the peridotite. Olivine hydration during early  
996 hydrothermal alteration and obduction formed Fe(II,III) serpentine, Fe(II) brucite and hydrogen.  
997 During the current phase of low temperature water/rock interaction, brucite is destabilized in the  
998 fluids with high  $\text{SiO}_2$  activity, generating  $\text{H}_2$  when it is converted to magnetite and additional  
999 Fe(III)-rich serpentine. The relict olivine is also further reacting to form Fe(III)-rich serpentine  
1000 and hydrogen. The formation mechanism for methane remains enigmatic, and could involve low  
1001 temperature abiotic  $\text{CO}_2$  reduction by mineral catalysts, or in-situ biological activity.

1002 Our study of drill cuttings and fluids reveals that the timing and extent of various stages of  
1003 serpentinization in Oman remain unconstrained. It is difficult to tease apart mineral parageneses  
1004 formed during hydrothermal alteration near an oceanic spreading ridge, emplacement of the  
1005 ophiolite, Late Cretaceous weathering, and modern water/rock reactions. Future studies that can  
1006 connect rock alteration histories along reaction paths with varying fluid sources and residence  
1007 times will be a valuable next step in assessing the mechanisms and extent of modern, low-  
1008 temperature  $\text{H}_2$  and  $\text{CH}_4$  generation. Continuous physical and magnetic properties measurements  
1009 downhole and on bulk core samples will help delineating sections with hydrology in situ where  
1010 serpentinization has been extensive.

1011 16s rRNA data of DNA extracted from the hyperalkaline fluid microbial communities indicate  
1012 an abundance of both aerobic and anaerobic organisms, including abundant *Meiothermus*,  
1013 *Thermodesulfovibrionaceae* (sulfate-reducers), Clostridia (fermentors), and *Hydrogenophaga*  
1014 ( $\text{H}_2$ -oxidizers). Although not abundant, methanogen *Methanobacterium* and candidate phylum  
1015 OP1 are also notably present. We hypothesize that the subsurface microbial communities are  
1016 harnessing the  $\text{H}_2$  produced by water/rock reactions, and coupling the oxidation of  $\text{H}_2$  to electron  
1017 acceptors such as  $\text{SO}_4^{2-}$ ,  $\text{CO}_2$  and Fe(III)-bearing phases at depth, and episodically with  $\text{O}_2$  and  
1018 nitrate in the upper fractured part of the aquifer.

1019 Probing the microbial community composition in these fluids provides a first glimpse into the  
1020 complex subsurface peridotite-hosted microbiome. The rock-hosted communities may be quite  
1021 different than those established in the fluids, due to strong gradients in redox potential, electron  
1022 acceptor and donor availability, porosity, permeability, fluid residence times, and mineral  
1023 reactivity. Moreover, this initial 16S rRNA gene sequence data are just an initial perspective  
1024 within the broader efforts to fully understand feedbacks between microbial activity, aqueous  
1025 geochemistry and mineralogy. Isolating and culturing the peridotite-hosted organisms will be an  
1026 important step in understanding their true metabolic activities and how they adapt to the carbon-  
1027 depleted, hyperalkaline fluid environment. The microorganisms may be utilizing carbonate veins  
1028 as a carbon source, leading to mineral dissolution and potential methane production.

1029 Additionally, microbial consumption of hydrogen from water/rock reactions may increase the  
1030 rate of hydrogen-producing reactions. Furthermore, in-situ microbes may be generating distinct  
1031 organic, mineral and/or isotopic biosignatures in serpentinizing environments that can be used to  
1032 identify microbial activity remotely.

1033 Examining the functional activity of microbial life in the subsurface will be important to fully  
1034 understand the coupling between the water/rock reactions, production of reduced gases, and  
1035 changes in aquifer chemistry and hydrology. A next step for studying the coupling between the  
1036 hydrological and geochemical processes and the distribution and activity of subsurface microbial  
1037 life will be to focus on process rate measurements of in-situ hydrogen generation and  
1038 consumption, pathways of C assimilation and uptake, and rates of methanogenesis, sulfate  
1039 reduction, and nitrate reduction. Intensive culturing of peridotite-adapted microorganisms in the  
1040 laboratory will also be necessary to elucidate the operative metabolic pathways. All of these  
1041 efforts will be greatly facilitated by the International Continental Drilling Program (ICDP)  
1042 project in Oman ([https://www.ldeo.columbia.edu/gpg/projects/icdp-workshop-oman-drilling-](https://www.ldeo.columbia.edu/gpg/projects/icdp-workshop-oman-drilling-project)  
1043 [project](https://www.ldeo.columbia.edu/gpg/projects/icdp-workshop-oman-drilling-project)). The results from this scientific endeavor will give further insight into predicted  
1044 mineralogy, microbiology, gas generation and C cycling of planetary systems undergoing active  
1045 alteration of peridotite in the shallow subsurface.

1046 **Acknowledgements:** The authors would like to thank Tori Hoehler and Mike Kubo (NASA  
1047 Ames) for providing exploratory organic acid analyses; Said Nasser Al-Habsi and Salim  
1048 Mohammed Al Khanbashi of the Ministry of Regional Municipalities and Water Resources  
1049 Sultanate of Oman for granting access to well fluids and drill cuttings; Amelia Paukert for  
1050 providing supporting information and samples. We would also like to thank numerous colleagues  
1051 at the University of Colorado at Boulder: Julien Allaz and the electron microprobe lab, the  
1052 Raman lab, Fred Luiszer at the Laboratory for Environmental and Geological Studies, the Barger  
1053 lab with their total organic carbon analyzer, the Fierer lab for their sequencing help, Lisa  
1054 Mayhew for valued discussions and Kaitlin Rempfert for help collecting samples in 2015.  
1055 Raman imaging and spectroscopy was conducted at the Raman Microspectroscopy Laboratory at  
1056 the Department of Geological Sciences, University of Colorado-Boulder. Use of the Stanford  
1057 Synchrotron Radiation Lightsource, SLAC National Accelerator Laboratory, is supported by the  
1058 U.S. Department of Energy, Office of Science, Office of Basic Energy Sciences under Contract  
1059 No. DE-AC02-76SF00515, in collaboration with staff scientists Sam Webb, Courtney Krest, and  
1060 Ryan Davis. This research was funded by the Department of Energy (DE-SC0006886), the  
1061 University of Colorado, the NASA Astrobiology Institute (Cooperative Agreement  
1062 NNA15BB02A), Alfred P. Sloan Foundation Grant 2014-3-01, and NSF EAR-1049905.

1063

1064

1065 **References**

- 1066 Abrajano T. A., Sturchio N. C., Kennedy B. M., Lyon G. L., Muehlenbachs K. and Bohlke J. K.  
1067 (1990) Geochemistry of reduced gas related to serpentinization of the Zambales ophiolite,  
1068 Philippines. *Appl. Geochem.* **5**, 625–630.
- 1069 Anderson R. T., Chapelle F. H. and Lovley D. R. (1998) Evidence Against Hydrogen-Based  
1070 Microbial Ecosystems in Basalt Aquifers. *Science* **281**, 976–977.
- 1071 Andreani M., Muñoz M., Marcaillou C. and Delacour A. (2013a)  $\mu$ XANES study of iron redox  
1072 state in serpentine during oceanic serpentinization. *Lithos* **178**, 70–83.
- 1073 Andreani M., Muñoz M., Marcaillou C. and Delacour A. (2013b)  $\mu$ XANES study of iron redox  
1074 state in serpentine during oceanic serpentinization. *Lithos* **178**, 70–83.
- 1075 Bach W., Paulick H., Garrido C. J., Ildefonse B., Meurer W. P. and Humphris S. E. (2006)  
1076 Unraveling the sequence of serpentinization reactions: petrography, mineral chemistry,  
1077 and petrophysics of serpentinites from MAR 15°N (ODP Leg 209, Site 1274). *Geophys.*  
1078 *Res. Lett.* **33**. Available at: <http://doi.wiley.com/10.1029/2006GL025681> [Accessed May  
1079 19, 2015].
- 1080 Balch W. E., Fox G. E., Magrum L. J., Woese C. R. and Wolfe R. S. (1979) Methanogens:  
1081 reevaluation of a unique biological group. *Microbiol. Rev.* **43**, 260–296.
- 1082 Barberán A., Ladau J., Leff J. W., Pollard K. S., Menninger H. L., Dunn R. R. and Fierer N.  
1083 (2015) Continental-scale distributions of dust-associated bacteria and fungi. *Proc. Natl.*  
1084 *Acad. Sci.* **112**, 5756–5761.
- 1085 Barnes I., LaMarche V. C. and Himmelberg G. (1967) Geochemical Evidence of Present-Day  
1086 Serpentinization. *Science* **156**, 830–832.
- 1087 Barnes I. and O’Neil J. R. (1969) The Relationship between Fluids in Some Fresh Alpine-Type  
1088 Ultramafics and Possible Modern Serpentinization, Western United States. *Geol. Soc.*  
1089 *Am. Bull.* **80**, 1947–1960.
- 1090 Barnes I., O’Neil J. R. and Trescases J. J. (1978) Present day serpentinization in New Caledonia,  
1091 Oman and Yugoslavia. *Geochim. Cosmochim. Acta* **42**, 144–145.
- 1092 Bottinga Y. (1969) Calculated fractionation factors for carbon and hydrogen isotope exchange in  
1093 the system calcite-carbon dioxide-graphite-methane-hydrogen-water vapor. *Geochim.*  
1094 *Cosmochim. Acta* **33**, 49–64.
- 1095 Boudier F., Baronnet A. and Mainprice D. (2010) Serpentine Mineral Replacements of Natural  
1096 Olivine and their Seismic Implications: Oceanic Lizardite versus Subduction-Related  
1097 Antigorite. *J. Petrol.* **51**, 495–512.

- 1098 Bowers R. M., Clements N., Emerson J. B., Wiedinmyer C., Hannigan M. P. and Fierer N.  
1099 (2013) Seasonal Variability in Bacterial and Fungal Diversity of the Near-Surface  
1100 Atmosphere. *Environ. Sci. Technol.* **47**, 12097–12106.
- 1101 Brazelton W. J., Morrill P. L., Szponar N. and Schrenk M. O. (2013) Bacterial Communities  
1102 Associated with Subsurface Geochemical Processes in Continental Serpentinite Springs.  
1103 *Appl. Environ. Microbiol.* **79**, 3906–3916.
- 1104 Brazelton W. J., Nelson B. and Schrenk M. O. (2012) Metagenomic Evidence for H<sub>2</sub> Oxidation  
1105 and H<sub>2</sub> Production by Serpentinite-Hosted Subsurface Microbial Communities. *Front.*  
1106 *Microbiol.* **2**. Available at:  
1107 <http://www.frontiersin.org/Journal/10.3389/fmicb.2011.00268/full> [Accessed January 30,  
1108 2014].
- 1109 Bruni J., Canepa M., Chiodini G., Cioni R., Cipolli F., Longinelli A., Marini L., Ottonello G. and  
1110 Vetuschi Zuccolini M. (2002) Irreversible water–rock mass transfer accompanying the  
1111 generation of the neutral, Mg–HCO<sub>3</sub> and high-pH, Ca–OH spring waters of the Genova  
1112 province, Italy. *Appl. Geochem.* **17**, 455–474.
- 1113 Butler R. and Banerjee S. (1975) Theoretical Single-Domain Grain Size Range in Magnetite and  
1114 Titanomagnetite. *J. Geophys. Res.*, 4049–4058.
- 1115 Cardace D. and Hoehler T. M. (2009) Serpentinizing Fluids Create Microbial Habitat. *Northeast.*  
1116 *Nat.* **16**, 272–284.
- 1117 Cardace D., Meyer-Dombard D. R., Woycheese K. M. and Arcilla C. A. (2015) Feasible  
1118 metabolisms in high pH springs of the Philippines. *Front. Microbiol.* **6**. Available at:  
1119 <http://journal.frontiersin.org/Article/10.3389/fmicb.2015.00010/abstract> [Accessed May  
1120 21, 2015].
- 1121 Chappelle F. H., O’Neill K., Bradley P. M., Methé B. A., Ciuffo S. A., Knobel L. L. and Lovley D.  
1122 R. (2002) A hydrogen-based subsurface microbial community dominated by  
1123 methanogens. *Nature* **415**, 312–315.
- 1124 Chavagnac V., Ceuleneer G., Monnin C., Lansac B., Hoareau G. and Boulart C. (2013)  
1125 Mineralogical assemblages forming at hyperalkaline warm springs hosted on ultramafic  
1126 rocks: A case study of Oman and Ligurian ophiolites. *Geochem. Geophys. Geosystems*  
1127 **14**, 2474–2495.
- 1128 Chavagnac V., Monnin C., Ceuleneer G., Boulart C. and Hoareau G. (2013) Characterization of  
1129 hyperalkaline fluids produced by low-temperature serpentinization of mantle peridotites  
1130 in the Oman and Ligurian ophiolites. *Geochem. Geophys. Geosystems* **14**, 2496–2522.
- 1131 Clark I. D. and Fontes J.-C. (1990) Paleoclimatic reconstruction in northern Oman based on  
1132 carbonates from hyperalkaline groundwaters. *Quat. Res.* **33**, 320–336.
- 1133 Coleman R. G. (1981) Tectonic setting for ophiolite obduction in Oman. *J. Geophys. Res. Solid*  
1134 *Earth* **86**, 2497–2508.

- 1135 Dewandel B., Lachassagne P., Boudier F., Al-Hattali S., Ladouche B., Pinault J.-L. and Al-  
1136 Suleimani Z. (2005) A conceptual hydrogeological model of ophiolite hard-rock aquifers  
1137 in Oman based on a multiscale and a multidisciplinary approach. *Hydrogeol. J.* **13**, 708–  
1138 726.
- 1139 Dunlop D. J. (1973) Superparamagnetic and single-domain threshold sizes in magnetite. *J.*  
1140 *Geophys. Res.* **78**, 1780–1793.
- 1141 Edgar R. C. (2013) UPARSE: highly accurate OTU sequences from microbial amplicon reads.  
1142 *Nat. Methods* **10**, 996–8.
- 1143 Emerson J. B., Keady P. B., Brewer T. E., Clements N., Morgan E. E., Awerbuch J., Miller S. L.  
1144 and Fierer N. (2015) Impacts of Flood Damage on Airborne Bacteria and Fungi in Homes  
1145 after the 2013 Colorado Front Range Flood. *Environ. Sci. Technol.* **49**, 2675–2684.
- 1146 Etiope G., Ehlmann B. L. and Schoell M. (2013) Low temperature production and exhalation of  
1147 methane from serpentinized rocks on Earth: A potential analog for methane production  
1148 on Mars. *Icarus* **224**, 276–285.
- 1149 Etiope G., Schoell M. and Hosgörmez H. (2011) Abiotic methane flux from the Chimaera seep  
1150 and Tekirova ophiolites (Turkey): Understanding gas exhalation from low temperature  
1151 serpentinization and implications for Mars. *Earth Planet. Sci. Lett.* **310**, 96–104.
- 1152 Etiope G. and Sherwood Lollar B. (2013) Abiotic Methane on Earth. *Rev. Geophys.* **51**, 276–  
1153 299.
- 1154 Evans B. W. (2010) Lizardite versus antigorite serpentinite: Magnetite, hydrogen, and life (?).  
1155 *Geology* **38**, 879–882.
- 1156 Evans B. W. (2004) The Serpentinite Multisystem Revisited: Chrysotile Is Metastable. *Int. Geol.*  
1157 *Rev.* **46**, 479–506.
- 1158 Evans B. W., Kuehner S. M. and Chopelas A. (2009) Magnetite-free, yellow lizardite  
1159 serpentinization of olivine websterite, Canyon Mountain complex, N.E. Oregon. *Am.*  
1160 *Mineral.* **94**, 1731–1734.
- 1161 Frost B. R. (1985) On the stability of sulfides, oxides, and native metals in serpentinite. *J. Petrol.*  
1162 **26**, 31–63.
- 1163 Frost B. R. and Beard J. S. (2007) On Silica Activity and Serpentinization. *J. Petrol.* **48**, 1351–  
1164 1368.
- 1165 Groppo C., Rinaudo C., Cairo S., Gastaldi D. and Compagnoni R. (2006) Micro-Raman  
1166 spectroscopy for a quick and reliable identification of serpentine minerals from  
1167 ultramafics. *Eur. J. Mineral.* **18**, 319–329.
- 1168 Hanghøj K., Kelemen P. B., Hassler D. and Godard M. (2010) Composition and Genesis of  
1169 Depleted Mantle Peridotites from the Wadi Tayin Massif, Oman Ophiolite; Major and

- 1170 Trace Element Geochemistry, and Os Isotope and PGE Systematics. *J. Petrol.* **51**, 201–  
1171 227.
- 1172 Haouari O., Fardeau M.-L., Cayol J.-L., Fauque G., Casiot C., Elbaz-Poulichet F., Hamdi M. and  
1173 Ollivier B. (2008) Thermodesulfovibrio hydrogeniphilus sp. nov., a new thermophilic  
1174 sulphate-reducing bacterium isolated from a Tunisian hot spring. *Syst. Appl. Microbiol.*  
1175 **31**, 38–42.
- 1176 Haroon M. F., Hu S., Shi Y., Imelfort M., Keller J., Hugenholtz P., Yuan Z. and Tyson G. W.  
1177 (2013) Anaerobic oxidation of methane coupled to nitrate reduction in a novel archaeal  
1178 lineage. *Nature* **500**, 567–570.
- 1179 Hicks D. B., Liu J., Fujisawa M. and Krulwich T. A. (2010) F1F0-ATP synthases of alkaliphilic  
1180 bacteria: Lessons from their adaptations. *Biochim. Biophys. Acta BBA - Bioenerg.* **1797**,  
1181 1362–1377.
- 1182 Hoehler T. M., Alperin M. J., Albert D. B. and Martens C. S. (1994) Field and laboratory studies  
1183 of methane oxidation in an anoxic marine sediment: Evidence for a methanogen-sulfate  
1184 reducer consortium. *Glob. Biogeochem. Cycles* **8**, 451–463.
- 1185 Horibe Y. and Craig H. (1995) DH fractionation in the system methane-hydrogen-water.  
1186 *Geochim. Cosmochim. Acta* **59**, 5209–5217.
- 1187 Horita J. and Berndt M. E. (1999) Abiogenic Methane Formation and Isotopic Fractionation  
1188 Under Hydrothermal Conditions. *Science* **285**, 1055–1057.
- 1189 Hug L. A., Castelle C. J., Wrighton K. C., Thomas B. C., Sharon I., Frischkorn K. R., Williams  
1190 K. H., Tringe S. G. and Banfield J. F. (2013) Community genomic analyses constrain the  
1191 distribution of metabolic traits across the Chloroflexi phylum and indicate roles in  
1192 sediment carbon cycling. *Microbiome* **1**, 22.
- 1193 Jacquemin M., Beuls A. and Ruiz P. (2010) Catalytic production of methane from CO<sub>2</sub> and H<sub>2</sub>  
1194 at low temperature: Insight on the reaction mechanism. *Catal. Today* **157**, 462–466.
- 1195 Joye S. B., Boetius A., Orcutt B. N., Montoya J. P., Schulz H. N., Erickson M. J. and Lugo S. K.  
1196 (2004) The anaerobic oxidation of methane and sulfate reduction in sediments from Gulf  
1197 of Mexico cold seeps. *Chem. Geol.* **205**, 219–238.
- 1198 Kelemen P. B. and Hirth G. (2012) Reaction-driven cracking during retrograde metamorphism:  
1199 Olivine hydration and carbonation. *Earth Planet. Sci. Lett.* **345–348**, 81–89.
- 1200 Kelemen P. B. and Matter J. (2008) In situ carbonation of peridotite for CO<sub>2</sub> storage. *Proc. Natl.*  
1201 *Acad. Sci.* **105**, 17295–17300.
- 1202 Kelemen P. B., Matter J., Streit E. E., Rudge J. F., Curry W. B. and Blusztajn J. (2011) Rates and  
1203 Mechanisms of Mineral Carbonation in Peridotite: Natural Processes and Recipes for  
1204 Enhanced, in situ CO<sub>2</sub> Capture and Storage. *Annu. Rev. Earth Planet. Sci.* **39**, 545–576.



- 1205 Klein F., Bach W., Humphris S. E., Kahl W.-A., Jons N., Moskowitz B. and Berquo T. S. (2013)  
1206 Magnetite in seafloor serpentinite--Some like it hot. *Geology* **42**, 135–138.
- 1207 Klein F., Bach W., Jöns N., McCollom T., Moskowitz B. and Berquó T. (2009) Iron partitioning  
1208 and hydrogen generation during serpentinization of abyssal peridotites from 15°N on the  
1209 Mid-Atlantic Ridge. *Geochim. Cosmochim. Acta* **73**, 6868–6893.
- 1210 Klein F., Bach W. and McCollom T. M. (2013) Compositional controls on hydrogen generation  
1211 during serpentinization of ultramafic rocks. *Lithos* **178**, 55–69.
- 1212 Klein F., Humphris S. E., Guo W., Schubotz F., Schwarzenbach E. M. and Orsi W. D. (2015)  
1213 Fluid mixing and the deep biosphere of a fossil Lost City-type hydrothermal system at the  
1214 Iberia Margin. *Proc. Natl. Acad. Sci.*, 201504674.
- 1215 Kumar M. R. and Saravanan V. S. (2011) Candidate OP Phyla: Importance, Ecology and  
1216 Cultivation Prospects. *Indian J. Microbiol.* **50**, 474–477.
- 1217 Lafay R., Montes-Hernandez G., Janots E., Chiriach R., Findling N. and Toche F. (2012) Mineral  
1218 replacement rate of olivine by chrysotile and brucite under high alkaline conditions. *J.*  
1219 *Cryst. Growth* **347**, 62–72.
- 1220 Laier T. and Nytoft H. P. (2012) Bitumen biomarkers in the Mid-Proterozoic Ilímaussaq  
1221 intrusion, Southwest Greenland – A challenge to the mantle gas theory. *Mar. Pet. Geol.*  
1222 **30**, 50–65.
- 1223 Lang S. Q., Butterfield D. A., Schulte M., Kelley D. S. and Lilley M. D. (2010) Elevated  
1224 concentrations of formate, acetate and dissolved organic carbon found at the Lost City  
1225 hydrothermal field. *Geochim. Cosmochim. Acta* **74**, 941–952.
- 1226 Lorand J. (1987) A New Occurrence of Native Iron in a Serpentinized Mantle Peridotite -  
1227 Maqsad, Sumail Massif, Semail Ophiolite (Southern Oman). *Comptes Rendus Acad. Sci.*  
1228 **Ii 304**, 703–6.
- 1229 Madigan M. T. (2012) *Brock biology of microorganisms.*, Benjamin Cummings, San Francisco.
- 1230 Malvoisin B., Carlut J. and Brunet F. (2012) Serpentinization of oceanic peridotites: 1. A high-  
1231 sensitivity method to monitor magnetite production in hydrothermal experiments. *J.*  
1232 *Geophys. Res. Solid Earth* **117**, B01104.
- 1233 Marcaillou C., Muñoz M., Vidal O., Parra T. and Harfouche M. (2011) Mineralogical evidence  
1234 for H<sub>2</sub> degassing during serpentinization at 300 °C/300 bar. *Earth Planet. Sci. Lett.* **303**,  
1235 281–290.
- 1236 Mayhew L. E., Ellison E. T., McCollom T. M., Trainor T. P. and Templeton A. S. (2013)  
1237 Hydrogen generation from low-temperature water–rock reactions. *Nat. Geosci.* **6**, 478–  
1238 484.

- 1239 Mayhew L. E., Webb S. M. and Templeton A. S. (2011) Microscale Imaging and Identification  
1240 of Fe Speciation and Distribution during Fluid–Mineral Reactions under Highly  
1241 Reducing Conditions. *Environ. Sci. Technol.* **45**, 4468–4474.
- 1242 McCollom T. M. and Bach W. (2009) Thermodynamic constraints on hydrogen generation  
1243 during serpentinization of ultramafic rocks. *Geochim. Cosmochim. Acta* **73**, 856–875.
- 1244 McCollom T. M. and Seewald J. S. (2001) A reassessment of the potential for reduction of  
1245 dissolved CO<sub>2</sub> to hydrocarbons during serpentinization of olivine. *Geochim. Cosmochim.*  
1246 *Acta* **65**, 3769–3778.
- 1247 McDonald D., Price M. N., Goodrich J., Nawrocki E. P., DeSantis T. Z., Probst A., Andersen G.  
1248 L., Knight R. and Hugenholtz P. (2012) An improved Greengenes taxonomy with explicit  
1249 ranks for ecological and evolutionary analyses of bacteria and archaea. *ISME J.* **6**, 610–8.
- 1250 Ménez B., Pasini V. and Brunelli D. (2012) Life in the hydrated suboceanic mantle. *Nat. Geosci.*  
1251 **5**, 133–137.
- 1252 Mervine E. M., Humphris S. E., Sims K. W. W., Kelemen P. B. and Jenkins W. J. (2014)  
1253 Carbonation rates of peridotite in the Samail Ophiolite, Sultanate of Oman, constrained  
1254 through <sup>14</sup>C dating and stable isotopes. *Geochim. Cosmochim. Acta* **126**, 371–397.
- 1255 Meyer-Dombard D. R., Woycheese K. M., YargÄ±ÄoÄlu E. N., Cardace D., Shock E. L.,  
1256 GÄ¼leÄal-Pektas Y. and Temel M. (2015) High pH microbial ecosystems in a newly  
1257 discovered, ephemeral, serpentinizing fluid seep at YanartaÄ (Chimera), Turkey. *Front.*  
1258 *Microbiol.* **5**. Available at:  
1259 <http://journal.frontiersin.org/article/10.3389/fmicb.2014.00723/abstract> [Accessed March  
1260 7, 2015].
- 1261 Moody J. B. (1976) Serpentinization: a review. *Lithos* **9**, 125–138.
- 1262 Morrill P. L., Kuenen J. G., Johnson O. J., Suzuki S., Rietze A., Sessions A. L., Fogel M. L. and  
1263 Neilson K. H. (2013) Geochemistry and geobiology of a present-day serpentinization site  
1264 in California: The Cedars. *Geochim. Cosmochim. Acta* **109**, 222–240.
- 1265 Mulkidjanian A. Y., Dibrov P. and Galperin M. Y. (2008) The past and present of sodium  
1266 energetics: May the sodium-motive force be with you. *Biochim. Biophys. Acta BBA -*  
1267 *Bioenerg.* **1777**, 985–992.
- 1268 MuÄoz M., Vidal O., Marcaillou C., Pascarelli S., Mathon O. and Farges F. (2013) Iron  
1269 oxidation state in phyllosilicate single crystals using Fe-K pre-edge and XANES  
1270 spectroscopy: Effects of the linear polarization of the synchrotron X-ray beam. *Am.*  
1271 *Mineral.* **98**, 1187–1197.
- 1272 Neal C. and Stanger G. (1984) Calcium and magnesium hydroxide precipitation from alkaline  
1273 groundwaters in Oman, and their significance to the process of serpentinization. *Miner.*  
1274 *Mag* **48**, 237–241.

- 1275 Neal C. and Stanger G. (1983) Hydrogen generation from mantle source rocks in Oman. *Earth*  
1276 *Planet. Sci. Lett.* **66**, 315–320.
- 1277 Neal C. and Stanger G. (1985) Past And Present Serpentinisation of Ultramafic Rocks; An  
1278 Example from the Semail Ophiolite Nappe of Northern Oman. In *The Chemistry of*  
1279 *Weathering* (ed. J. I. Drever). Nato ASI Series. Springer Netherlands. pp. 249–275.  
1280 Available at: [http://link.springer.com/chapter/10.1007/978-94-009-5333-8\\_15](http://link.springer.com/chapter/10.1007/978-94-009-5333-8_15) [Accessed  
1281 June 17, 2015].
- 1282 Nealson K. H., Inagaki F. and Takai K. (2005) Hydrogen-driven subsurface lithoautotrophic  
1283 microbial ecosystems (SLiMEs): do they exist and why should we care? *Trends*  
1284 *Microbiol.* **13**, 405–410.
- 1285 Neubeck A., Duc N. T., Bastviken D., Crill P. and Holm N. G. (2011) Formation of H<sub>2</sub> and CH<sub>4</sub>  
1286 by weathering of olivine at temperatures between 30 and 70 C. *Geochem. Trans.* **12**, 6.
- 1287 Nielsen J. L. and Nielsen P. H. (1998) Microbial Nitrate-Dependent Oxidation of Ferrous Iron in  
1288 Activated Sludge. *Environ. Sci. Technol.* **32**, 3556–3561.
- 1289 Okland I., Huang S., Dahle H., Thorseth I. H. and Pedersen R. B. (2012) Low temperature  
1290 alteration of serpentinized ultramafic rock and implications for microbial life. *Chem.*  
1291 *Geol.* **318-319**, 75–87.
- 1292 Pasini V., Brunelli D., Dumas P., Sandt C., Frederick J., Benzerara K., Bernard S. and Ménez B.  
1293 (2013) Low temperature hydrothermal oil and associated biological precursors in  
1294 serpentinites from Mid-Ocean Ridge. *Lithos* **178**, 84–95.
- 1295 Paukert A. N., Matter J. M., Kelemen P. B., Shock E. L. and Havig J. R. (2012) Reaction path  
1296 modeling of enhanced in situ CO<sub>2</sub> mineralization for carbon sequestration in the  
1297 peridotite of the Semail Ophiolite, Sultanate of Oman. *Chem. Geol.* **330-331**, 86–100.
- 1298 Petriglieri J. R., Salvioli-Mariani E., Mantovani L., Tribaudino M., Lottici P. P., Laporte-Magoni  
1299 C. and Bersani D. (2015) Micro-Raman mapping of the polymorphs of serpentine. *J.*  
1300 *Raman Spectrosc.*, n/a–n/a.
- 1301 Postec A., Quéméneur M., Bes M., Mei N., Benaïssa F., Payri C., Pelletier B., Monnin C.,  
1302 Guentas-Dombrowsky L., Ollivier B., Gérard E., Pisapia C., Gérard M., Ménez B. and  
1303 Erauso G. (2015) Microbial diversity in a submarine carbonate edifice from the  
1304 serpentinizing hydrothermal system of the Prony Bay (New Caledonia) over a 6-year  
1305 period. *Front. Microbiol.* **6**. Available at:  
1306 <http://www.ncbi.nlm.nih.gov/pmc/articles/PMC4551099/> [Accessed November 20,  
1307 2015].
- 1308 Proskurowski G., Lilley M. D., Kelley D. S. and Olson E. J. (2006) Low temperature volatile  
1309 production at the Lost City Hydrothermal Field, evidence from a hydrogen stable isotope  
1310 geothermometer. *Chem. Geol.* **229**, 331–343.

- 1311 R Development Core Team (2008) *R: A language and environment for statistical computing.*, R  
1312 Foundation for Statistical Computing, Vienna, Austria. Available at: [http://www.R-](http://www.R-project.org)  
1313 [project.org](http://www.R-project.org).
- 1314 Ravaut P., Bayer R., Hassani R., Rousset D. and Yahya'ey A. A. (1997) Structure and evolution  
1315 of the northern Oman margin: gravity and seismic constraints over the Zagros-Makran-  
1316 Oman collision zone. *Tectonophysics* **279**, 253–280.
- 1317 Rinaudo C., Gastaldi D. and Belluso E. (2003) Characterization of Chrysotile, Antigorite and  
1318 Lizardite by Ft-Raman Spectroscopy. *Can. Mineral.* **41**, 883–890.
- 1319 Schrenk M. O., Brazelton W. J. and Lang S. Q. (2013) Serpentinization, Carbon, and Deep Life.  
1320 *Rev. Mineral. Geochem.* **75**, 575–606.
- 1321 Sherwood Lollar B., Frape S. K., Weise S. M., Fritz P., Macko S. A. and Welhan J. A. (1993)  
1322 Abiogenic methanogenesis in crystalline rocks. *Geochim. Cosmochim. Acta* **57**, 5087–  
1323 5097.
- 1324 Sleep N. H., Meibom A., Fridriksson T., Coleman R. G. and Bird D. K. (2004) H<sub>2</sub>-rich fluids  
1325 from serpentinization: geochemical and biotic implications. *Proc. Natl. Acad. Sci. U. S.*  
1326 *A.* **101**, 12818–12823.
- 1327 Stanger G. (1986) The hydrogeology of the Oman Mountains. Open University London.
- 1328 Stevens T. O. and McKinley J. P. (2000) Abiotic Controls on H<sub>2</sub> Production from Basalt–Water  
1329 Reactions and Implications for Aquifer Biogeochemistry. *Environ. Sci. Technol.* **34**, 826–  
1330 831.
- 1331 Stevens T. O. and McKinley J. P. (1995) Lithoautotrophic Microbial Ecosystems in Deep Basalt  
1332 Aquifers. *Science* **270**, 450–455.
- 1333 Streit E., Kelemen P. and Eiler J. (2012) Coexisting serpentine and quartz from carbonate-  
1334 bearing serpentinized peridotite in the Samail Ophiolite, Oman. *Contrib. Mineral. Petrol.*  
1335 **164**, 821–837.
- 1336 Suzuki S., Ishii S., Wu A., Cheung A., Tenney A., Wanger G., Kuenen J. G. and Nealson K. H.  
1337 (2013) Microbial diversity in The Cedars, an ultrabasic, ultrareducing, and low salinity  
1338 serpentinizing ecosystem. *Proc. Natl. Acad. Sci.* **110**, 15336–15341.
- 1339 Suzuki S., Kuenen J. G., Schipper K., van der Velde S., Ishii S., Wu A., Sorokin D. Y., Tenney  
1340 A., Meng X., Morrill P. L., Kamagata Y., Muyzer G. and Nealson K. H. (2014)  
1341 Physiological and genomic features of highly alkaliphilic hydrogen-utilizing  
1342 Betaproteobacteria from a continental serpentinizing site. *Nat. Commun.* **5**. Available at:  
1343 <http://www.nature.com/ncomms/2014/140521/ncomms4900/full/ncomms4900.html>  
1344 [Accessed November 19, 2014].
- 1345 Takami H., Noguchi H., Takaki Y., Uchiyama I., Toyoda A., Nishi S., Chee G.-J., Arai W.,  
1346 Nunoura T., Itoh T., Hattori M. and Takai K. (2012) A Deeply Branching Thermophilic

- 1347 Bacterium with an Ancient Acetyl-CoA Pathway Dominates a Subsurface Ecosystem.  
1348 *PLoS ONE* **7**, e30559.
- 1349 Tauxe L., Banerjee S. K., Butler R. F. and van der Voo R. (2014) Essentials of Paleomagnetism,  
1350 3rd Web Edition.
- 1351 Telling J., Boyd E. S., Bone N., Jones E. L., Tranter M., MacFarlane J. W., Martin P. G.,  
1352 Wadham J. L., Lamarche-Gagnon G., Skidmore M. L., Hamilton T. L., Hill E., Jackson  
1353 M. and Hodgson D. A. (2015) Rock comminution as a source of hydrogen for subglacial  
1354 ecosystems. *Nat. Geosci.* **8**, 851–855.
- 1355 Templeton A. S., Chu K.-H., Alvarez-Cohen L. and Conrad M. E. (2006) Variable carbon  
1356 isotope fractionation expressed by aerobic CH<sub>4</sub>-oxidizing bacteria. *Geochim.*  
1357 *Cosmochim. Acta* **70**, 1739–1752.
- 1358 Tindall B. J., Sikorski J., Lucas S., Goltsman E., Copeland A., Glavina Del Rio T., Nolan M.,  
1359 Tice H., Cheng J.-F., Han C., Pitluck S., Liolios K., Ivanova N., Mavromatis K.,  
1360 Ovchinnikova G., Pati A., Föhnrich R., Goodwin L., Chen A., Palaniappan K., Land M.,  
1361 Hauser L., Chang Y.-J., Jeffries C. D., Rohde M., Göker M., Woyke T., Bristow J., Eisen  
1362 J. A., Markowitz V., Hugenholtz P., Kyrpides N. C., Klenk H.-P. and Lapidus A. (2010)  
1363 Complete genome sequence of *Meiothermus ruber* type strain (21T). *Stand. Genomic Sci.*  
1364 **3**, 26–36.
- 1365 Wang Q., Garrity G. M., Tiedje J. M. and Cole J. R. (2007) Naive Bayesian classifier for rapid  
1366 assignment of rRNA sequences into the new bacterial taxonomy. *Appl. Environ.*  
1367 *Microbiol.* **73**, 5261–7.
- 1368 Weyhenmeyer C. (2000) Origin and evolution of groundwaters in the alluvial aquifer of the  
1369 Eastern Batinah Coastal Plain, Sultanate of Oman. *PhD Thesis Univ. Bern Switz.*
- 1370 Whiticar M. J. (1990) A geochemical perspective of natural gas and atmospheric methane. *Org.*  
1371 *Geochem.* **16**, 531–547.
- 1372 Whiticar M. J. (1999) Carbon and hydrogen isotope systematics of bacterial formation and  
1373 oxidation of methane. *Chem. Geol.* **161**, 291–314.
- 1374 Whiticar M. J. and Faber E. (1986) Methane oxidation in sediment and water column  
1375 environments—Isotope evidence. *Org. Geochem.* **10**, 759–768.
- 1376 Wilke M., Farges F., Petit P.-E., Brown G. E. and Martin F. (2001) Oxidation state and  
1377 coordination of Fe in minerals: An Fe K-XANES spectroscopic study. *Am. Mineral.* **86**,  
1378 714–730.
- 1379 Willems A., Busse J., Goor M., Pot B., Falsen E., Jantzen E., Hoste B., Gillis M., Kersters K.,  
1380 Auling G. and others (1989) *Hydrogenophaga*, a new genus of hydrogen-oxidizing  
1381 bacteria that includes *Hydrogenophaga flava* comb. nov. (formerly *Pseudomonas flava*),  
1382 *Hydrogenophaga palleronii* (formerly *Pseudomonas palleronii*), *Hydrogenophaga*  
1383 *pseudoflava* (formerly *Pseudomonas pseudoflava* and “*Pseudomonas carboxydoflava*”),

- 1384 and *Hydrogenophaga taeniospiralis* (formerly *Pseudomonas taeniospiralis*). *Int. J. Syst.*  
1385 *Bacteriol.* **39**, 319–333.
- 1386 Worm H.-U. (1998) On the superparamagnetic—stable single domain transition for magnetite,  
1387 and frequency dependence of susceptibility. *Geophys. J. Int.* **133**, 201–206.
- 1388 Woycheese K. M., Meyer-Dombard D. R., Cardace D., Argayosa A. M. and Arcilla C. A. (2015)  
1389 Out of the dark: transitional subsurface-to-surface microbial diversity in a terrestrial  
1390 serpentinizing seep (Manleluag, Pangasinan, the Philippines). *Front. Microbiol.* **6**.  
1391 Available at: <http://journal.frontiersin.org/Article/10.3389/fmicb.2015.00044/abstract>  
1392 [Accessed May 21, 2015].
- 1393
- 1394

1395 **Table 1.** Major and minor elements in wells along with pH, temperature, and conductivity.  
 1396 Oman hyperalkaline spring data is from Paukert et al. (2012) sampling Type II surface waters.  
 1397 Oxidation-reduction potential (ORP) data is from sampling the wells in 2012. Gas concentrations  
 1398 were determined by measuring the headspace of anaerobic vials purged with N<sub>2</sub> filled with site  
 1399 water.

	<b>NSHQ04 18meters</b>	<b>NSHQ14 18meters</b>	<b>NSHQ14 260meters</b>	<b>Misbit - Oman hyperalkaline spring</b>
pH	10.6	11.1	11.5	11.2
Temperature (°C)	33.3	34.3	31.5	31.6
Conductivity (µS/m)	2386	2430	4300	1640
ORP (mV)	-103.4 (70m)	-31.6	-597.3	-
Na <sup>+</sup> (mM)	12.136	12.302	6.747	2.120
Ca <sup>2+</sup> (mM)	6.424	7.604	9.001	0.017
Mg <sup>2+</sup> (mM)	0.005	0.060	0.655	6.540
K <sup>+</sup> (mM)	0.409	0.422	0.361	-
SiO <sub>2(aq)</sub> (mM)	0.011	0.007	0.016	0.040
Cl <sup>-</sup> (mM)	24.942	25.932	21.848	6.970
SO <sub>4</sub> <sup>2-</sup> (mM)	0.483	0.190	0.050	0.070
NO <sub>3</sub> <sup>-</sup> (mM)	0.012	0.022	0.016	<0.01
Br <sup>-</sup> (mM)	0.001	<0.001	0.001	-
Al <sup>3+</sup> (mM)	0.098	0.086	0.045	0.023
Fe <sup>2+</sup> (mM)	<0.001	<0.001	<0.001	<0.001
DIC (mM)	0.091	0.078	0.391	-
H <sub>2</sub> (mM)	0.18	0.67	0.17	-
CH <sub>4</sub> (mM)	1.44	0.17	0.04	-
Ni (µM)	0.147	0.137	0.156	-
As (µM)	0.042	0.04	0.047	-
Se (µM)	0.094	0.144	0.166	-
Cu (µM)	0.032	0.04	0.045	-
Cd (µM)	<8.90E-05	<8.90E-05	<8.90E-05	-
Zn (µM)	0.028	0.056	0.139	-
Co (µM)	0.006	0.005	0.007	-
Cr (µM)	0.163	0.17	0.19	-

1401 **Table 2.**  $\delta D$  H<sub>2</sub>,  $\delta^{13}C$  CH<sub>4</sub>, and  $\delta D$  CH<sub>4</sub> values for subsurface well water in Oman (NSHQ04 and  
 1402 NSHQ14), as well as hyperalkaline surface springs in Oman (Neal and Stanger, 1983), Zambales  
 1403 Ophiolite in the Philippines (Abrajano et al., 1990), Lost City Hydrothermal Vents  
 1404 (Proskurowski et al., 2006), the Precambrian Canadian Shield (Sherwood Lollar et al., 1993),  
 1405 and the Cedars Ophiolite in California (Morrill et al., 2013).

	$\delta D$ H <sub>2</sub> ‰	$\delta D$ CH <sub>4</sub> ‰	$\delta^{13}C$ CH <sub>4</sub> ‰
NSHQ04_18m	-680	-205	2.4
NSHQ14_262m	-685	-232	3
Nizwa, Oman	-697		
Bahla, Oman	-699		
Huwayl Qufays, Oman	-699		
B'lad, Oman	-714		
Zambales Ophiolite	-581	-122	-7.34
Lost City Hydrothermal Vents	-609	-127	-10
Precambrian Canadian Shield	-619	-284	-29
Cedars ophiolite	-40 to -50		-68

1406

1407



1408 **Table 3.**  $\delta^{13}\text{C}$  and  $\delta^{18}\text{O}$  values from carbonate found in drill cuttings. The unreported values are  
1409 due to low carbonate concentrations.

	$\delta^{13}\text{C}_{\text{VPDB}}$	$\delta^{18}\text{O}_{\text{VPDB}}$
NSHQ14_17m	-7.05	-7.73
NSHQ14_70m	--	--
NSHQ14_140m	-4.75	-11.07
NSHQ14_262m	-4.69	-11.49
NSHQ04_120m	--	--
NSHQ04_180m	--	--
NSHQ04_303m	-1.48	-10.99

1410

1411 **Table 4.** Electron microprobe weight % data for serpentine generations from well chip  
 1412 NSHQ04\_180m corresponding to varying generations of serpentine identified with Raman  
 1413 spectroscopy. Numbers refer to various analysis spots on the well chip thin section.

<b>Generation 1 and 2 chrysotile (04-gen1,2)</b>						
<b>Sample</b>	<b>3</b>	<b>5</b>	<b>6</b>	<b>9</b>	<b>10</b>	<b>average</b>
<b>Na<sub>2</sub>O</b>	0.00	0.00	0.00	0.00	0.04	0.01
<b>MgO</b>	36.41	35.22	36.17	36.86	35.63	36.06
<b>Al<sub>2</sub>O<sub>3</sub></b>	0.40	0.99	0.82	0.31	0.85	0.67
<b>SiO<sub>2</sub></b>	38.21	35.97	36.40	36.70	37.05	36.87
<b>CaO</b>	0.40	0.54	0.44	0.30	0.47	0.43
<b>FeO</b>	7.29	8.50	7.51	8.12	8.20	7.92
<b>MnO</b>	0.20	0.26	0.18	0.14	0.32	0.22
<b>TiO<sub>2</sub></b>	0.00	0.00	0.00	0.00	0.00	0.00
<b>Cr<sub>2</sub>O<sub>3</sub></b>	0.09	0.61	0.51	0.00	0.42	0.33
<b>Total</b>	82.99	82.09	82.03	82.43	82.99	82.51
<b>Mg #</b>	0.83	0.81	0.83	0.82	0.81	0.82

<b>Generation 3 lizardite intermixed with brucite (04-gen3)</b>						
<b>Sample</b>	<b>7</b>	<b>8</b>	<b>11</b>	<b>12</b>	<b>13</b>	<b>average</b>
<b>Na<sub>2</sub>O</b>	0.00	0.00	0.00	0.00	0.00	0.00
<b>MgO</b>	41.00	41.01	40.93	40.74	40.84	40.90
<b>Al<sub>2</sub>O<sub>3</sub></b>	0.00	0.00	0.08	0.14	0.03	0.05
<b>SiO<sub>2</sub></b>	33.58	34.51	35.74	34.63	34.54	34.60
<b>CaO</b>	0.06	0.07	0.12	0.15	0.12	0.10
<b>FeO</b>	8.12	7.41	6.07	6.13	7.24	6.99
<b>MnO</b>	0.00	0.00	0.11	0.09	0.15	0.07
<b>TiO<sub>2</sub></b>	0.00	0.00	0.00	0.00	0.00	0.00
<b>Cr<sub>2</sub>O<sub>3</sub></b>	0.00	0.00	0.00	0.00	0.00	0.00
<b>Total</b>	82.76	83.00	83.05	81.88	82.93	82.72
<b>Mg #</b>	0.83	0.85	0.87	0.87	0.85	0.85

1414

1415